The Southern Ocean Waves Experiment. Part II: Sea Surface Response to Wind Speed and Wind Stress Variations

WEI CHEN AND MICHAEL L. BANNER

School of Mathematics, The University of New South Wales, Sydney, New South Wales, Australia

EDWARD J. WALSH*

Laboratory for Hydrospheric Processes, NASA Goddard Space Flight Center, Wallops Island, Virginia

JORGEN B. JENSEN AND SUNHEE LEE

CSIRO Atmospheric Research, Aspendale, Victoria, Australia

(Manuscript received 20 May 1999, in final form 31 March 2000)

ABSTRACT

The Southern Ocean Waves Experiment (SOWEX) was an international collaborative air–sea interaction experiment in which a specially instrumented meteorological research aircraft simultaneously gathered marine boundary-layer atmospheric turbulence data and sea surface roughness data over the Southern Ocean, particularly for gale-force wind conditions. In this paper analysis and findings are presented on key aspects of the coupled variability of the wind field, the wind stress, and the underlying sea surface roughness. This study complements the overview, methodology, and mean results published in Part I.

Weakly unstable atmospheric stratification conditions prevailed during SOWEX, with wind speeds ranging from gale force to light and variable. Throughout the SOWEX observational period, the wind field was dominated by large-scale atmospheric roll-cell structures, whose height scale was comparable with the thickness of the marine atmospheric boundary layer (MABL). Well above the sea surface, these coherent structures provide the dominant contribution to the downward momentum flux toward the sea surface. Closer to the sea surface, these organized large-scale structures continued to make significant contributions to the downward momentum flux, even within a few tens of meters of the sea surface.

At the minimum aircraft height, typical cumulative stress cospectra indicated that 10-km averages along crosswind tracks appeared adequate to close the stress cospectrum. Nevertheless, a large-scale spatial inhomogeneity in the wind stress vector was observed using 10- and 20-km spatial averaging intervals on one of the strongest wind days when the mean wind field was close to being spatially uniform. This indicates a departure from the familiar drag coefficient relationship and implies large-scale transverse modulations in the MABL with an effective horizontal to vertical aspect ratio of around 20.

A high visual correlation was found between mean wind speed variations and collocated sea-surface mean square slope (mss) variations, averaged over 1.9 km. A comparable plot of the 10-km running average of the downward momentum flux, observed at heights from 30 to 90 m, showed appreciably lower visual correlation with the wind speed variations and mss variations. The 10–20 km averaging distance needed to determine the wind stress was larger than the local scale of variation of the mss roughness variations. It also exceeded the scale of the striations often observed in synthetic aperture radar imagery under unstable atmospheric conditions and strong wind forcing. This highlights an overlooked intrinsic difficulty in using the friction velocity as the wind parameter in models of the wind wave spectrum, especially for the short wind wave scales.

1. Introduction

The wind stress over the ocean quantifies the complex dynamical coupling between the atmospheric wind field and the sea surface. Because of its central role in air–sea interaction, the wind stress and its drag coefficient have been studied intensively over the past few decades, with different investigators reporting significant variation among their observations of the drag coefficient dependence on wind speed. Due to the significant, if not dominant, role of wave form drag in the wind stress, the degree of development of the sea state provides one potential source of this variability, yet this dependence has not been easily resolved in drag coefficient measurements. While a few observational studies have reported evidence of wave age dependence in the drag

* Current affiliation: NOAA/Environmental Technology Laboratory, Boulder, Colorado.

Corresponding author address: Prof. Michael L. Banner, School of Mathematics, The University of New South Wales, Sydney 2052, Australia.
E-mail: m.banner@unsw.edu.au

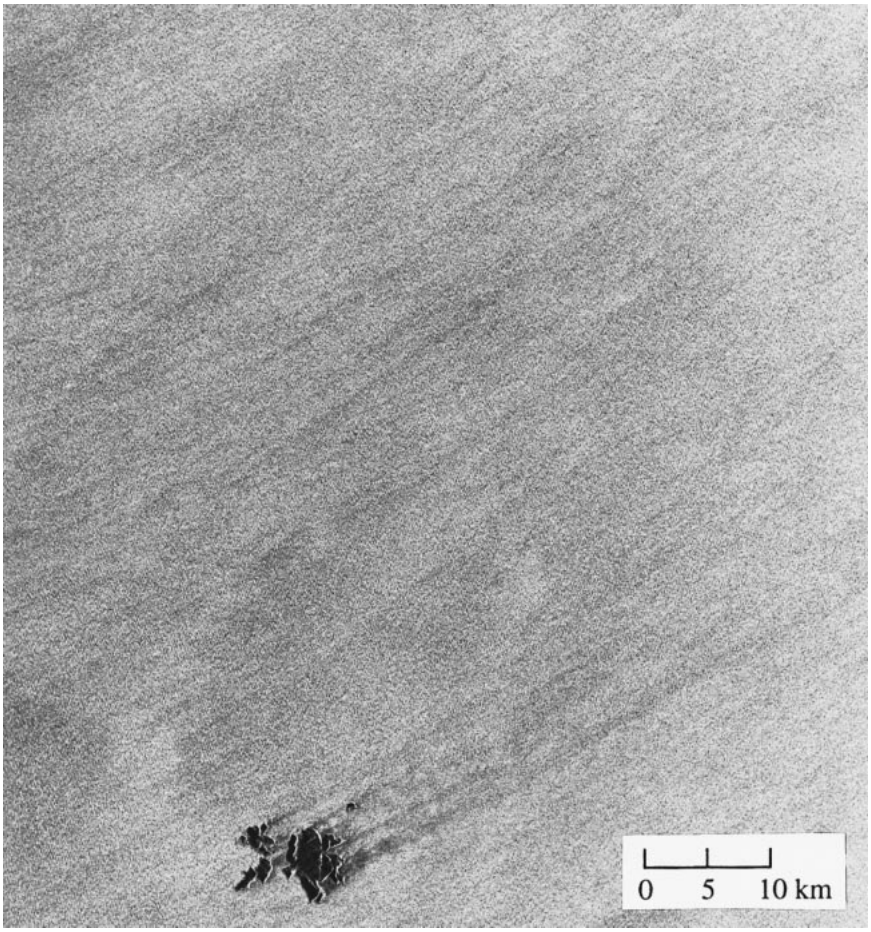

FIG. 1. *ERS-1* SAR image of the sea surface over Bass Strait (39°09′S, 147°20′E) on 11 Aug 1992, with $U_{10} = 17.6$ m s^{-1} and the wind from 245°. The longitudinal striations on the sea surface are aligned approximately in the wind direction. The darkened areas associated with sheltered flow in the lee of the small islands indicate that the dark striations in the image are regions of reduced mean surface wind speed.

coefficient primarily for short fetch and coastal sites, this behavior has been masked in the few open-ocean studies that reported data for a wide range of wave ages. The recent paper of Rieder and Smith (1998) provides very interesting insight into this question for open-ocean conditions involving complex seas. Thus sea state influence remains an important contemporary issue in air–sea interaction research.

Other spatial and temporal sources of variability of the wind stress are also under increasing scrutiny, through a combination of more detailed in situ observations (e.g., Rieder 1997) and spatially extensive observations from research aircraft and satelliteborne instruments. An illustration of variability of sea surface roughness observable in satellite imagery is shown in Fig. 1. This *ERS-1* synthetic aperture radar (SAR) image was taken one month after the Southern Ocean Waves Experiment (SOWEX) mission (described below) during quasi-steady 17.3 m s^{-1} gale-force winds from the southwest over the Bass Strait area adjacent to the Southern Ocean. This image reveals narrow longitudinal striation features aligned approximately in the wind direction, with a large streamwise coherence of O(100 km) and lateral spacings of O(1–5 km). Similar patterns have been reported previously (e.g., Fu and Holt 1982, Fig. 40). These SAR signatures reflect the variations in short wind wave energy density at the resonant Bragg wavenumber, in this case wind wavelets with wavelengths of approximately 50 mm. These systematic roughness modulations transverse to the wind direction are consistent with surface signatures of atmospheric roll-cell structures, whose common occurrence, particularly in unstably stratified atmospheric conditions, can be a significant source of variability in wind stress determinations from fixed platforms.

To better understand this and other sources of variability for open-ocean conditions with mixed windsea and swell, further investigation is needed on the wind stress and its relationship to the wind field and sea surface roughness, especially based on spatially extensive

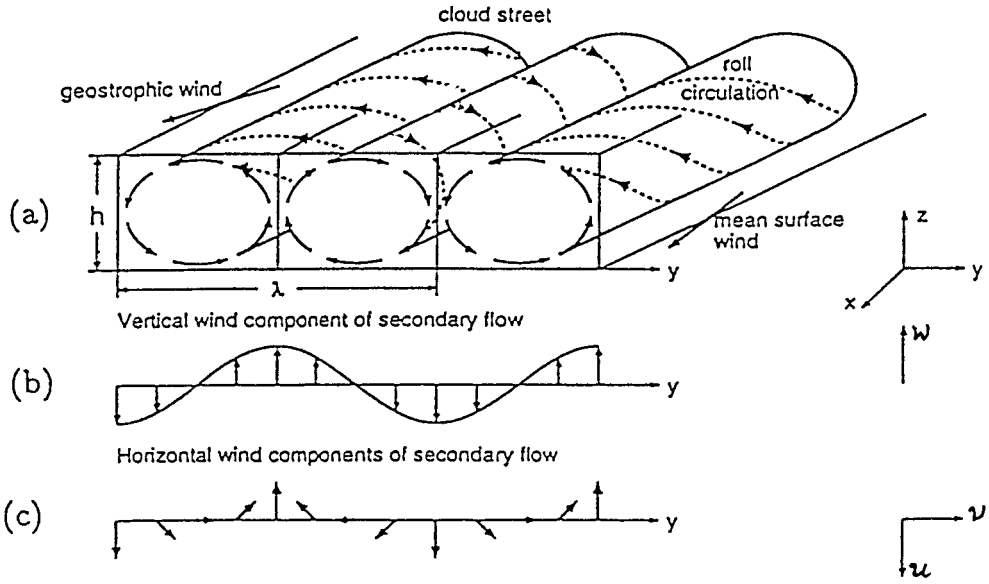

FIG. 2. Schematic diagram of atmospheric roll cells (a) three-dimensional perspective view, (b) transverse variation of the vertical component w of the wind velocity, and (c) transverse variation of the resultant of the horizontal velocity components u and v (after Alpers and Brummer 1994).

data. The fundamental issue of wind stress variability also depends on the choice of time and space scales used to average the turbulent stress cospectrum in the marine atmospheric boundary layer (MABL), and is an issue that appears to be more complex than is generally appreciated.

In this context, the SOWEX was an aircraft-based air–sea interaction measurement program conducted during 10–16 June 1992 over the Southern Ocean in the region [42°–45°S, 143°–147°E] off the southwest coast of Tasmania, Australia. Briefly, in SOWEX we deployed the NASA Scanning Radar Altimeter aboard the CSIRO F27 meteorological research aircraft. The available instrumentation allowed us to make atmospheric turbulence measurements in the marine surface boundary layer at the minimum elevation above the sea surface consistent with safety requirements during the wide range of wind conditions that prevailed. Simultaneous measurements were made of wave elevation and mean square slope (mss) as measures of sea surface roughness, providing observations of both upwind/downwind and crosswind variations over spatial scales O(80 km). A full description of the experiment, associated instrumentation, and mean flow results is given in Banner et al. (1999, henceforth SI). In the present paper, we report on the coupled variability among the wind field, wind forcing, and sea surface roughness.

2. Structure of the wind field in the marine boundary layer

a. Atmospheric roll vortices

Atmospheric roll vortices are large-scale helical circulations in the MABL seen frequently in satellite pictures as elongated cloud streaks. The degree of alignment of their axes with the mean wind direction depends on the atmospheric stability, with near-alignment tending to occur for unstable conditions. The schematic diagram in Fig. 2 illustrates their key features, particularly the systematic reduction in the local mean wind speed U corresponding to updraft regions. Throughout this paper, the wind fluctuations about the local mean wind velocity $\mathbf{U}$ are (u, v, w), where u is in the mean velocity direction, v is in the transverse direction, and w is vertically upward, as indicated in this figure. Earlier studies based on satellite images focused mostly on their occurrence and size (e.g., Brown 1980). From these satellite pictures, roll vortices can be found with lateral dimensions ranging from several hundred meters to several kilometers, extending longitudinally over several hundred kilometers. Their vertical extent spans the thickness of the MABL. Atmospheric roll vortices are often found in weakly unstable thermal conditions and may also occur in neutral conditions. Etling and Brown (1993) provide a recent comprehensive review of atmospheric roll vortices, including a detailed discussion on the possible underlying mechanisms of inflexion point instability, parallel instability, or convective instability.

Aircraft observations at different altitudes provide the possibility of increasing quantitative knowledge about the structure of atmospheric roll vortices and their influence on the vertical transport of momentum, heat, and moisture. From such observations over land, LeMone (1973) reported that the horizontal wavelength of atmospheric roll vortices varied from 1.5 km to 6.5 km, with the roll axes aligned from 10° to 20° to the left of the mean geostrophic wind direction (in the

Northern Hemisphere). LeMone (1976) also found systematic concentration of turbulent fluxes in ascending regions of the roll cells. Over the sea, Nicholls (1978) and Nicholls and Reading (1979, 1981) reported detailed results of aircraft measurements of velocity, temperature, and humidity fluctuations for alongwind and crosswind traverses close to the sea surface during unstable atmospheric conditions. In particular, Nicholls and Reading (1981) found distinctively different momentum flux cospectral signatures for these two flight traverse directions. They attributed this to an eddy stretching mechanism by the mean wind shear but also discussed the possibility of roll-cell influence. Brummer (1985) presented vertical profiles of the roll scale fluxes and total fluxes, together with their spectral distributions. These indicated that the roll-scale fluxes were maximized in the middle of the roll layer and nearly vanished at the sea surface and also at the top of the roll layer. From the measurements involving two aircraft flying at a number of levels in the MABL, he inferred that two of the three roll-cell episodes encountered during high wind, slightly unstable conditions were due to shear instability and the third was driven by thermal instability. In a recent large-eddy simulation numerical study of a case of cold air outbreak with large surface heat flux and strong wind shear, by partitioning the total vertical fluxes into the contribution of roll vortices and the contribution of nonroll turbulence, Glendening (1994) predicted stronger downward momentum fluxes within the ascending regions of the roll cells for both the mean (roll) momentum and the turbulent momentum.

In the above studies it was suggested that atmospheric roll vortices may be less important near the sea surface, but their potential influence on the near-surface wind stress and sea surface behavior has been recognized. Boyle et al. (1987) and Smith et al. (1992) proposed that such large-scale atmospheric structures influence the estimation of momentum flux and wind stress from fixed platforms, causing scatter in drag coefficient determinations. Gerling (1986) found a consistent peak at wavelengths of about 2 km in surface wave spectra obtained from satellite SAR images and attributed this organization of the flow to short-wave variability in response to wind speed modulations induced by atmospheric roll cells. Alpers and Brummer (1994) reported that the streaks visible on two *ERS-1* SAR images were aligned approximately in the wind direction and their spatial scales were close to the theoretical value for atmospheric roll vortices. The *ERS-1* SAR image shown in Fig. 1 indicates the presence of atmospheric roll-cell structures through the surface roughness modulations induced by the roll-cell influence at the sea surface. Clearly, their slow lateral drift across the mean wind direction makes roll cells potentially significant contributors to the variability in tower-based wind stress observations. More recently, Mourad and Walter (1996) and Mourad (1996) reported very interesting interpretations of multiscale structure in advanced very high resolution radiometer imagery and SAR imagery of cold air outbreaks. Mourad (1996) identified three nested scales of interacting atmospheric turbulence through their SAR image signatures in the MABL: compact ''islands'' of smaller scale (1 km wide, 2.5 km long), two-dimensional organized structures exist within the familiar larger scale roll vortices that persist for many tens of kilometers. Embedded within these compact two-dimensional structures are small-scale, active microfronts up to 100 m wide and several hundred meters in length. These modulated microfronts are associated with large contrasts in the SAR imagery and appear to be very active in the air–sea interfacial dynamics.

As documented in SI, the atmospheric stratification was weakly unstable throughout the SOWEX observational period and the inversion height on the different days varied from 600 to 1000 m. The stability parameter z/L at the aircraft height z ranged between -0.15 on the strongest gale-force wind day to -0.5 for the lowest wind speed day [L is the Monin-Obukhov stability length (see SI, sec. 1)]. For these relatively weak unstable stratification conditions, we investigated the presence of roll cells and their physical length scales by examining the crosswind flight track data for the v and w velocity components for a phase difference of close to $\pm 90°$. This phase relationship is specific to roll-cells and does not occur for random turbulence (Hein and Brown 1988). Further, as Fig. 2 illustrates, the v component leads the w component by about 90° during aircraft traverses across roll cells from right to left, and the v component lags about 90° behind the w component when the flight direction is from left to right.

Our standard flight path geometry comprised one upwind (u.w.) and two reverse crosswind (c.w.) legs relative to the wind, as close to the sea surface as possible, with another crosswind leg at twice that altitude. On some days, additional legs were flown, and the interested reader is referred to Table 2 in SI for full details. From the crosswind leg data, cross-spectral phase analysis of the velocity fluctuations established that atmospheric roll vortices occurred throughout SOWEX. From our flights at different altitudes, we were able to draw conclusions about the influence of roll cells on the wind field, their spectral contributions to the downward momentum flux at different altitudes, and their potential influence on the determination of mean wind speed and wind stress from fixed platforms. Details of these analyses are described below.

Figure 3 presents typical cross-spectral results of analyzing our velocity records at different flight levels in the MABL for evidence of the phase relationships that characterize coherent structures. Figures 3a–c show the corresponding coherence squared (γ^2) and phase angle between pairs of velocity components on three representative days for these different flight levels and directions: (a) 10 June: gale-force ($U_{10} \approx 20$ m s^{-1}) winds with mature windsea conditions; (b) 11 June: very

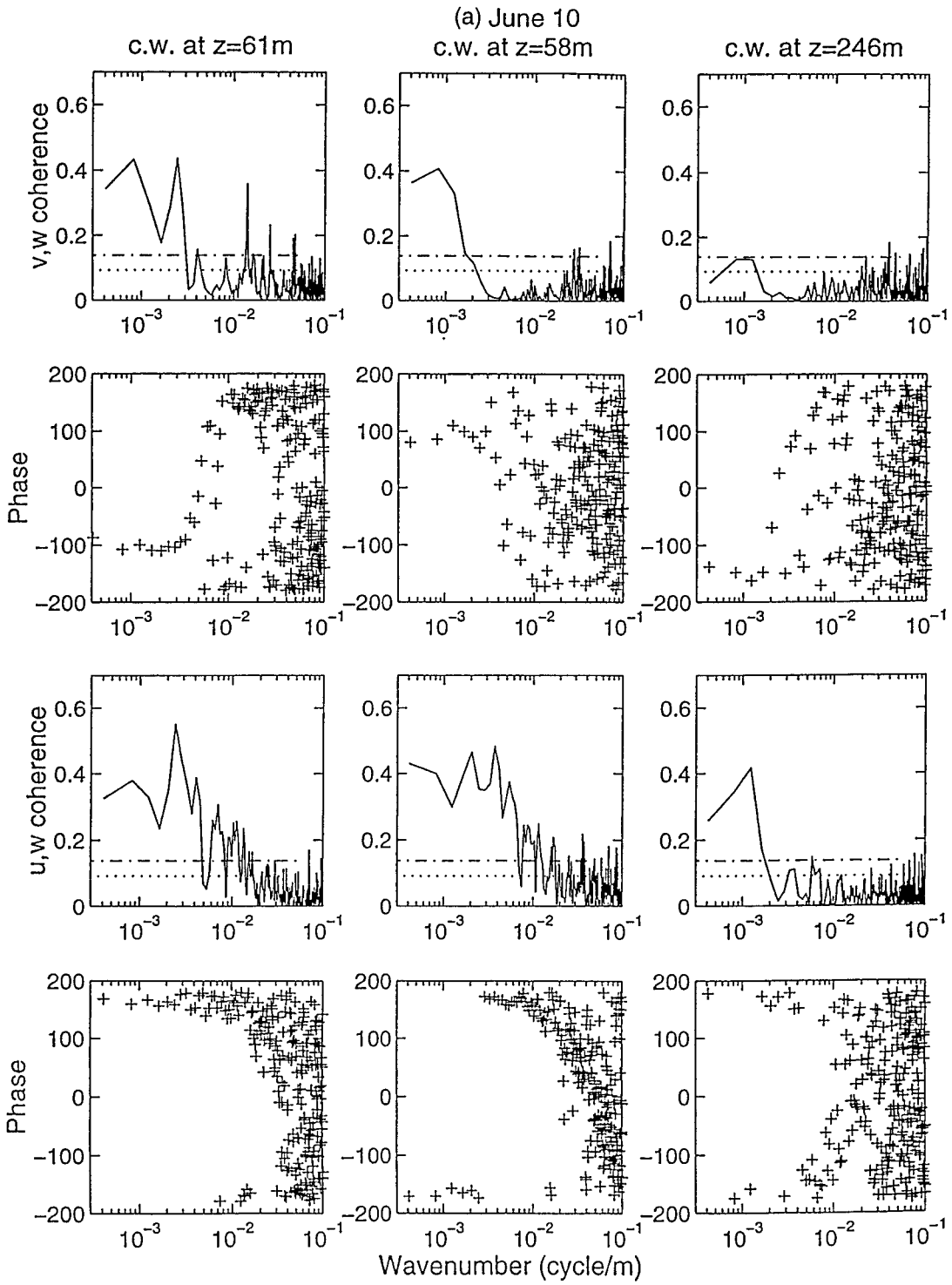

FIG. 3. Wavenumber cross-spectral phase analysis results for the wind fluctuations for three representative wind and sea state conditions. (a) 10 Jun: $U_{10} \approx 20$ m s^{-1}, 13.7-s wind waves with 9.2-m significant wave height; (b) 11 Jun: $U_{10} \sim 15$ m s^{-1}, 12.9-s swell waves with 4.2-m significant wave height; (c) 13 Jun: $U_{10} \sim 9$ m s^{-1}, 13.8-s swell waves with 4-m significant wave height. For any given day (a)–(c), each column corresponds to the indicated flight direction and altitude. In each column, the plots from top to bottom are: coherence (γ^2) between v and w, corresponding relative phase angle in

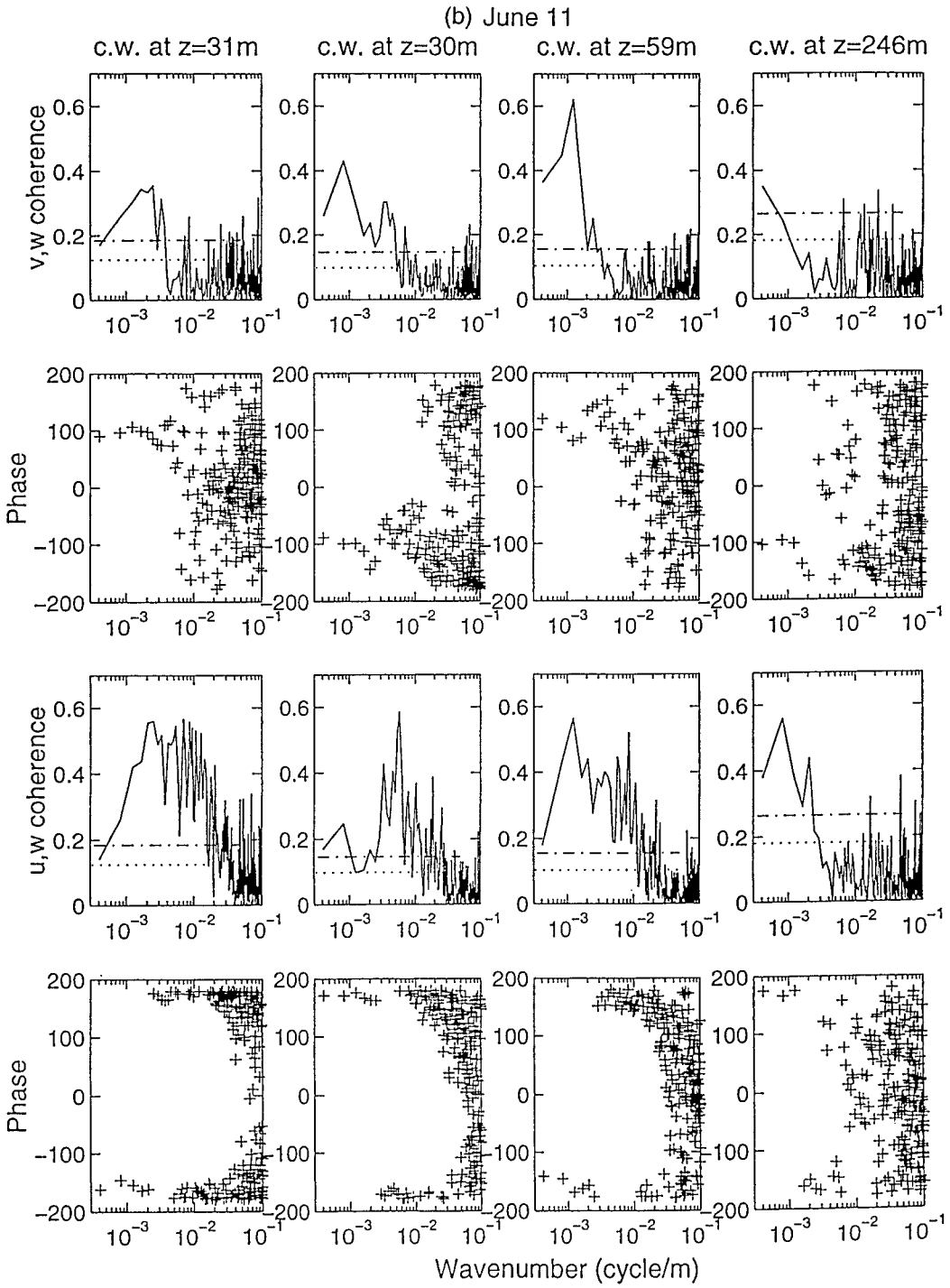

FIG. 3. (*Continued*) degrees between v and w, coherence between u and w, and corresponding relative phase angle in degrees between u and w. Crosswind and upwind traverses are indicated by ''c.w.'' and ''u.w.,'' respectively. The lowest level c.w. traverses were reverse legs. The 95% and 99% confidence limits for the coherence are shown, respectively, by dotted and dash–dotted lines.

strong winds ($U_{10} \approx 15$ m s^{-1}) in the presence of a codirectional 12.9 s, 4.2 m significant wave height swell; (c) 13 June: moderate winds ($U_{10} \approx 9$ m s^{-1}) with a codirectional 13.8 s, 4 m significant wave height swell. Consistent with the schematic roll-cell structure in Fig. 2, the v and w correlations (upper two panels in each figure) show that at each aircraft measurement level, the v and w components have close to 90° phase difference

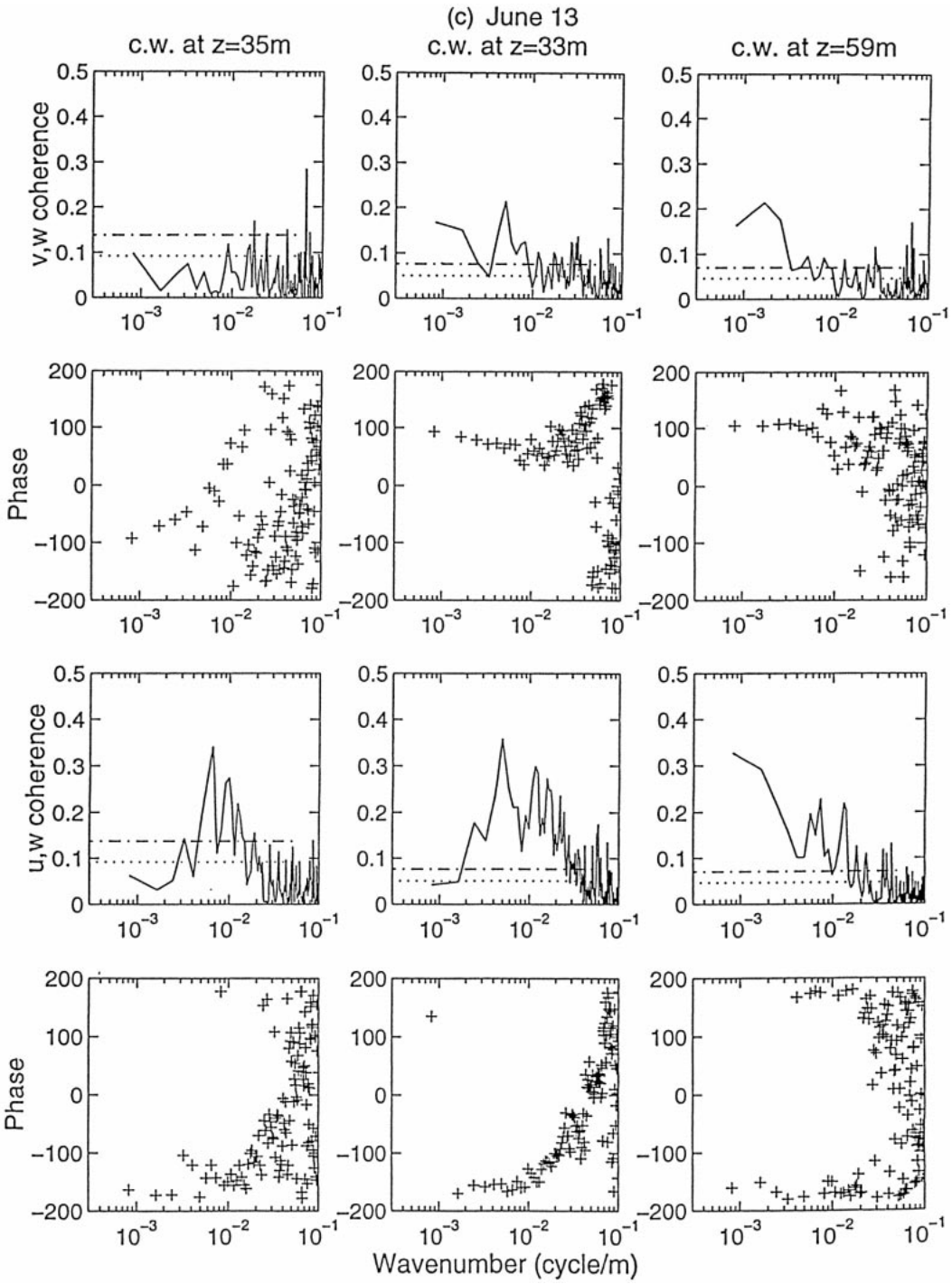

FIG. 3. (*Continued*)

over an appreciable range of length scales. In addition, the sign of the phase difference reverses for the return low-level crosswind flight track, thereby confirming the presence of roll cells.

The lower two panels in each of these figures show the corresponding phase-coherence results for the *u* and *w* components. These establish a clear antiphase ($\pm 180^\circ$) relationship for an even broader spectral subrange, implying that, on the average, the horizontal wind speed reduces within ascending regions of the flow and increases within descending regions.

The transverse velocity results confirm the presence of organized structures throughout SOWEX and provide information on their typical length scales. For example,

in Fig. 3b, at an elevation of 246 m, the coherent wavelength range with phase differences close to 90° is seen to extend from about 800 m toward longer wavelengths. At lower altitudes, this wavelength range extends from about 300 up to 2000 m. According to Fig. 3c, this correlation is seen less clearly for some measurement tracks during moderate winds. Overall, the presence of roll cells was detected over a significant range of length scales.

These coherent features of atmospheric roll structures were also visible in time series plots of the three velocity components of the crosswind measurements, particularly in the high-level crosswind measurements made at 246-m elevation where the random turbulent fluctuations have attenuated. The interested reader is referred to Chen (1997) for further details.

b. Spectral wind stress contributions

The traditional approach for studying the spectral structure of the wind stress is through interpretation of suitably weighted cospectra of u, v, and w, which reveal the mean contribution to the total momentum flux of any given spectral range of the fluctuating wind field. The k-weighted velocity wavenumber spectra and cospectra for different altitudes and flight directions of velocity measurements are shown for the corresponding days in Figs. 4a–c. It should be noted that the k weighting visually enhances the importance of higher wavenumber peaks. In each of these figures, the energy spectra for the u, v, and w velocity components are shown in the first three panels from the left. They are plotted in log–log form to highlight the presence, spectral levels, and wavenumber ranges of the inertial subrange ($k^{-5/3}$) structure for the higher wavenumber spectral components of the wind velocity. The momentum flux cospectra are shown in the rightmost set of panels in standard energy-preserving form as kS_{uw} and kS_{vw} plotted against $\log_{10}(k)$. In this format, the contribution to the momentum flux within any given fractional wavenumber (or wavelength) band is readily visualized.

For gale-force wind conditions, the momentum flux cospectra in the right-hand panels of Figs. 4a and 4b show that the alongwind component of momentum flux is much larger than the crosswind component for most wavelengths and dominates the total momentum flux. The crosswind track (c.w.) measurements shown in Figs. 4a and 4b reveal that the peak wavelength of the downward momentum flux contribution is about 1000 m at a height of 246 m. This peak wavelength reduces to about 250–330 m at the lowest observational heights of about 60 and 30 m respectively. However, the upwind track (u.w.) measurements shown in the bottom panel of Figs. 4a and 4b reveal that the momentum flux is dominated by scales larger than O(500 m), compared with scales of O(250 m) for the crosswind measurement at the same level. This anisotropic behavior was found for all gale-force wind days during SOWEX.

The same anisotropic behavior is seen in Fig. 4c for 13 June when $U_{10} \approx 9$ m s^{-1}. For 14 June, however, on the lowest wind speed day (not shown here) when $U_{10} \approx 6$ m s^{-1}, the wind direction showed much greater variability. The cospectra for these conditions indicate that the peak wavelength of $\langle -uw \rangle$ was about 100 m at heights of 20 and 38 m for crosswind tracks and was very similar for upwind/downwind measurements. This insensitivity to the sampling direction possibly reflects detuning of the organized flow structure in the directionally varying wind conditions that prevailed.

The significance of these unexpected findings of appreciable roll-cell contributions to the momentum flux cospectra very close to the sea surface is reviewed in section 4.

c. Intermittency of $-uw$ and the contribution of coherent structures in the MABL

It is well known that a random variable generated by the product of two Gaussian random variables shows strong intermittency, with sporadic occurrences of very large values. A familiar example is the behavior of the instantaneous product of two turbulent fluctuating velocity components in classical turbulent boundary-layer flows. As reviewed by Robinson (1991), laboratory studies of conditional statistics of the predominant turbulent Reynolds stress term $\langle -uw \rangle$ in conventional smooth wall turbulent boundary layers indicate that this stress component is dominated by so-called ''sweep'' events ($u > 0$, $w < 0$) in the viscous sublayer flow adjacent to the boundary and by ''ejection'' events ($u < 0$, $w > 0$) outside the viscous sublayer. The corresponding behavior in the unstable MABL is likely to be even more complex due to the combined influence of thermal instability and rotation of the surface-layer fluid overlying a mobile bounding surface. Indeed, intermittency in the $-uw$ signal has been noted routinely in previous aircraft turbulence studies over the sea (e.g., Nicholls 1978) when significant convective motions including atmospheric roll cells were present. This intermittency is also a prominent feature of the SOWEX dataset, and it is of interest here to examine briefly the influence of the presence of coherent MABL structures on the observed intermittency statistics of sweep and ejection events.

Visual inspection of the high aircraft altitude ($z =$ 246 m) SOWEX velocity data (Chen 1997, Fig. 3.15) reveals that large bursts in the local $-uw$ signal occur mainly in ascending regions of atmospheric roll cells, where the mean wind speed is systematically reduced. At this altitude, the presence of large-scale atmospheric roll structures appears to be the major source of the intermittency observed in $-uw$ at the aircraft height, with clear visual evidence of strong ejection-like events where $u < 0$ and $w > 0$. Much closer to the sea surface, in the range of $z = 30$–60 m, the visual correlation is less clear, but the phase-coherence data in Fig. 3 indicate

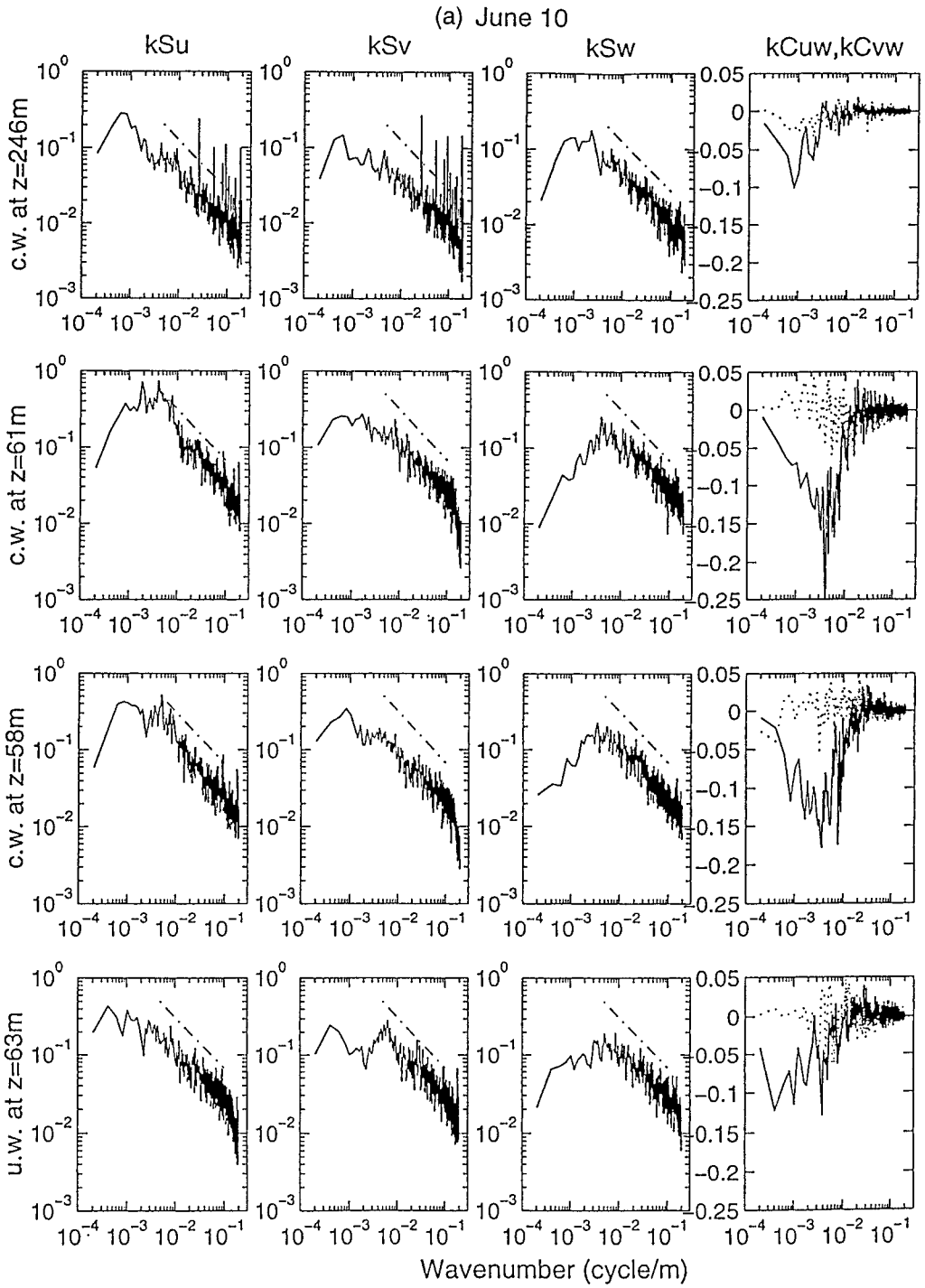

FIG. 4. Wavenumber spectral and cross-spectral amplitude analysis of the wind fluctuations for three representative wind and sea-state conditions. (a) 10 Jun: $U_{10} \approx 20$ m s^{-1}, 13.7-s wind waves with 9.2-m significant wave height; (b) 11 Jun: $U_{10} \approx 15$ m s^{-1}, 12.9-s swell waves with 4.2-m significant wave height; (c) 13 Jun: $U_{10} \approx 9$ m s^{-1}, 13.8-s swell waves with 4-m significant wave height. For any given day (a)–(c), each row is identified on the left by the flight altitude and direction. On the *y* axis ''c.w.'' denotes crosswind track and ''u.w.'' denotes upwind track.

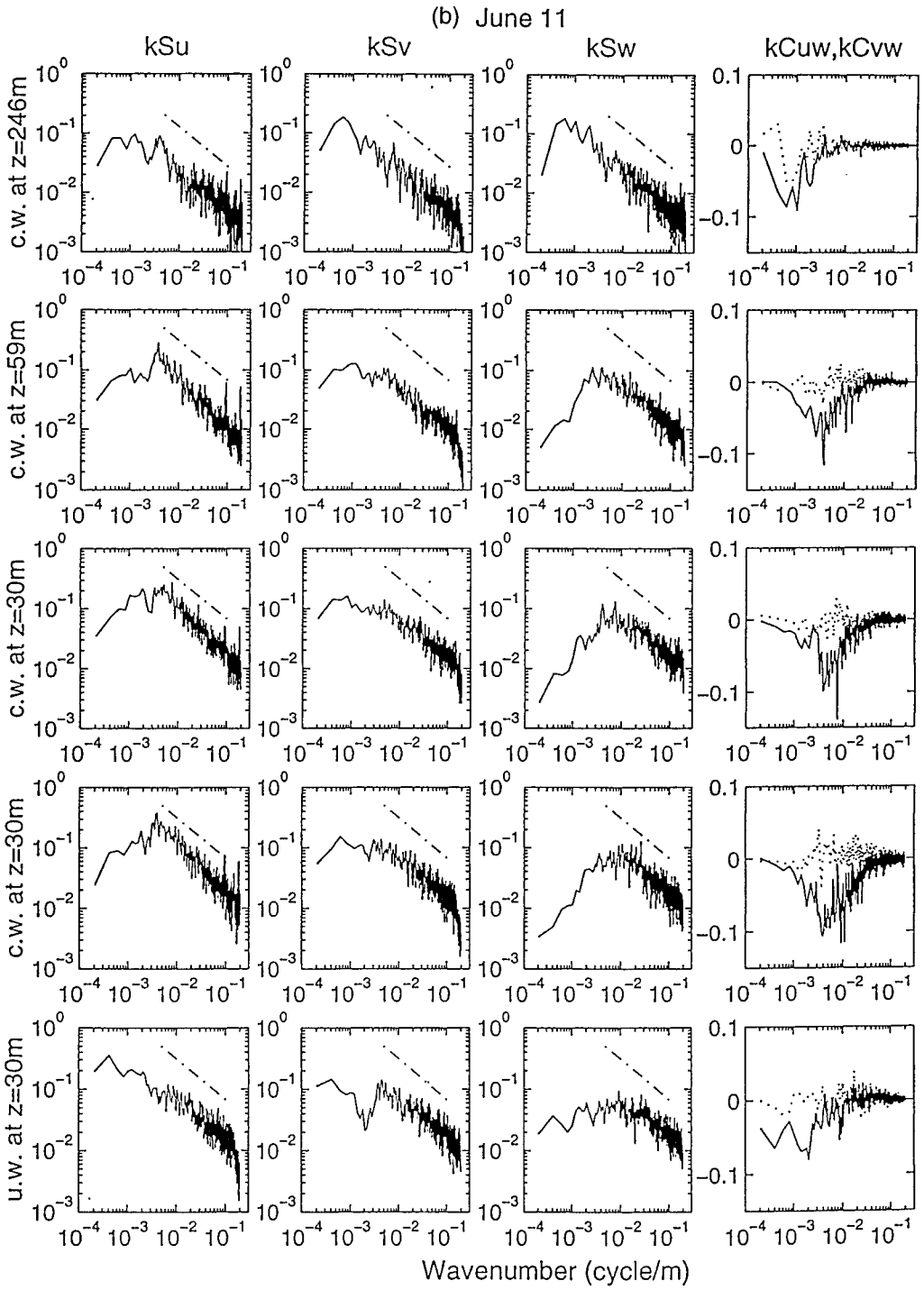

FIG. 4. (*Continued*) From left to right are shown: the k-weighted intensity spectra for u, v, w and cospectra for uw and vw. The inertial subrange behavior is indicated by the dash–dotted lines shown in the intensity spectra, which have slope $k^{-2/3}$ instead of $k^{-5/3}$ because of the k weighting. In the cospectral plots, the solid lines are cospectra of u and w; the dotted lines are cospectra of v and w. These plots are in area-preserving form.

that the coherent roll-cell structure persists for wavelengths of about 300 m and longer.

From the phase and turbulence intensity spectra in Figs. 3 and 4, the $\pm$ 180° signature in the u, w phase spectra for the near-surface measurements appear to persist to wavelengths as short as O(80 m). Interestingly, these short scales lie well within the $k^{-5/3}$ inertial subrange seen in the velocity fluctuation spectra. To better

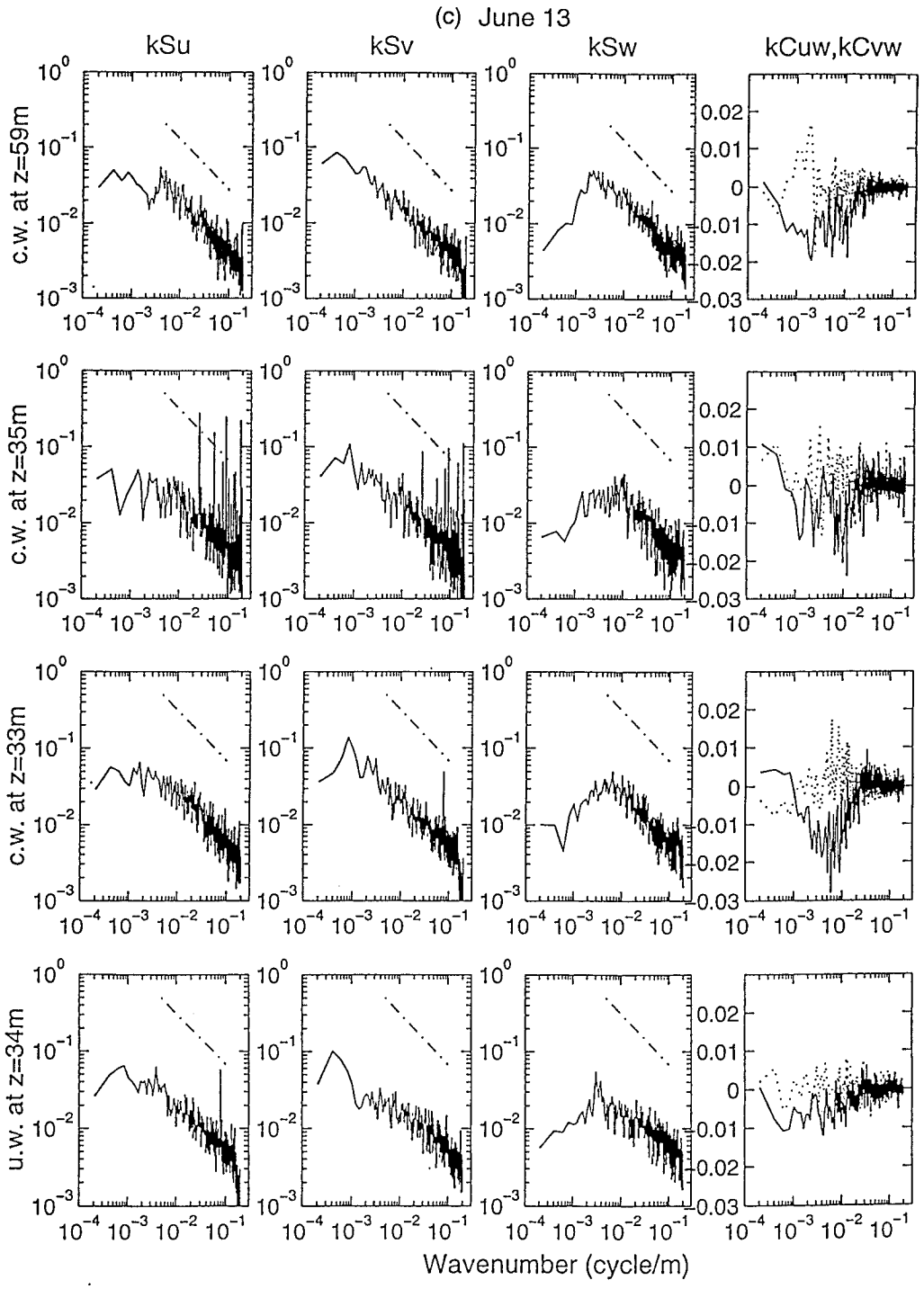

FIG. 4. (*Continued*)

understand the relative contributions of the organized roll-cell flow and sea-surface-generated turbulence, we decided to present intermittency data in the form of four quadrant contributions Q-I: ($u > 0$, $w > 0$), Q-II: ($u < 0$, $w > 0$), Q-III: ($u < 0$, $w < 0$), and Q-IV: ($u > 0$, $w < 0$).

Figures 5a and 5b present key aspects of these intermittency statistics for 10 June and 13 June respectively. These findings are typical of the other days. The upper pair of plots in Fig. 5a shows the full bandwidth results, while the center pair and the lowest pair of plots, respectively, show the same dataset after partitioning

into low and high wavenumber bands using a four-pole bidirectional Butterworth filter with a center wavelength of 300 m. This scale was chosen to represent the boundary between the inertial subrange and roll-cell structures, based on the low flight level data in Figs. 3 and 4. For each flight track and elevation, the left- and right-hand plots of each pair show, respectively, the proportion of data points in each quadrant over the entire track and the relative momentum flux contribution from each quadrant in the corresponding wavenumber band. We normalized using U_{10}^2 rather than $\langle -uw \rangle$, because the former was more consistent between different legs, especially on 13 June. The relative contribution of the low- and high-pass filtered $\langle -uw \rangle$ to the total wind stress may be assessed from the corresponding cospectra in Fig. 4.

Figure 5a shows momentum flux intermittency statistics for gale-force wind conditions on 10 June. The full spectral bandwidth data in the top left panel show that ascending events ($w > 0$) in Q-I and Q-II occur only 45% of the time. Furthermore, Q-II downward momentum flux events involving updrafts have a systematically lower spatial extent than Q-IV downdraft momentum flux events involving updrafts, at both 60 m and 246 m elevations, yet the top right panel shows that the Q-II events dominate the Q-I events, providing about two-thirds of the downward momentum flux contribution at 246-m elevation in this case. This ratio reduces only modestly toward the sea surface. Also, the upward momentum flux contributions from Q-I and Q-III are approximately equal and are significantly smaller than the downward momentum flux contributions. Remarkably, similar proportions of the momentum flux contributions in the four quadrants are seen at both 60-m and 246-m levels.

The central pair of plots in Fig. 5a shows the low-pass filtered data, revealing a similar trend for the event distribution as for the unfiltered data. The downward momentum flux ratio between Q-II and Q-IV events is comparable with the unfiltered data at the low elevation, but is now nearly three times greater at the higher elevation. The other two quadrant events (Q-I, Q-III) each make momentum flux contributions of similar magnitude to the Q-IV events, but of opposite sign.

The lowest two plots in Fig. 5a show the high-pass filtered data and reveal a different behavior for the shorter velocity fluctuation scales that include the inertial subrange of turbulence generated at the sea surface. For these scales, the spatial distribution statistics in the left-hand plot show an increased tendency toward equipartitioning at both flight levels. The right-hand plot shows that for these shorter scales, the Q-II events now make a downward momentum flux contribution similar to the Q-IV events. The other two quadrants (Q-I, Q-III) each make momentum flux contributions of similar magnitude to the Q-IV events, but of opposite sign.

The companion plots in Fig. 5b show both similarities and variations in these intermittency properties for the moderate wind day of 13 June 1992, when the mean wind speed U_{10} was 9 m s^{-1}. The event statistics are very similar, yet the momentum flux distributions show certain differences. For instance, the magnitude of the individual quadrant momentum fluxes now increase with altitude. While Q-II still provides the larger downward momentum flux contribution, there is now much less contrast between these two.

The close similarity between the bandpass filtered statistics and the full bandwidth statistics for each of these days confirms that the behavior of the roll cells dominates the reported full-bandwidth intermittency properties at 246 m. Their intermittency signature is still easily identified at the lowest flight levels close to the sea surface, consistent with the cospectral data in Fig. 4, further confirming our finding in section 2b that roll cells remain an important downward momentum flux mechanism even at these low altitudes.

Even closer to the sea surface, we speculate that the peak of the momentum flux cospectrum associated with the surface-generated turbulence continues to shift to shorter scales, in accordance with the trend of our crosswind track observations at different altitudes. This would also parallel the universal form discussed in Fig. 7 of Donelan (1990) in the context of alongwind measurements from fixed platforms, where any roll-cell influence is likely to be recorded as extremely low frequency disturbances, based on the very slow lateral drift of the roll cells relative to the mean wind direction. This is consistent with the very different peak wavenumbers observed in our alongwind and crosswind cospectra. In any event, a consequence of the interpretation of the SAR image striations seen in Fig. 1 is that the dynamical influence of the roll cells extends right down to the air–sea interface. An associated dynamical issue not addressed directly by our measurements is the relative contributions of momentum flux supported by the roll cells and surface-generated turbulence in such flows. Further discussion on this issue is taken up in section 4.

d. Averaging interval for the wind stress

The cumulative cospectrum (or ogive) has been used operationally to establish a suitable averaging interval for stationary estimates of momentum flux (Friehe et al. 1991). Figures 6a–f show cumulative cospectra for the magnitude of the vector combination of the alongwind and crosswind momentum flux components plotted against the wavelength for various traverses on 10, 11, and 13 June. These plots show the integrated momentum flux contribution from all scales of motion smaller than a given wavelength.

Figure 6a shows the absolute level of the cumulative cospectra for 10 June, while Fig. 6b shows this level normalized by the total momentum flux. The latter facilitates comparison of relative contributions of different length scales from different traverse levels and directions. During gale-force wind conditions, Fig. 6b shows

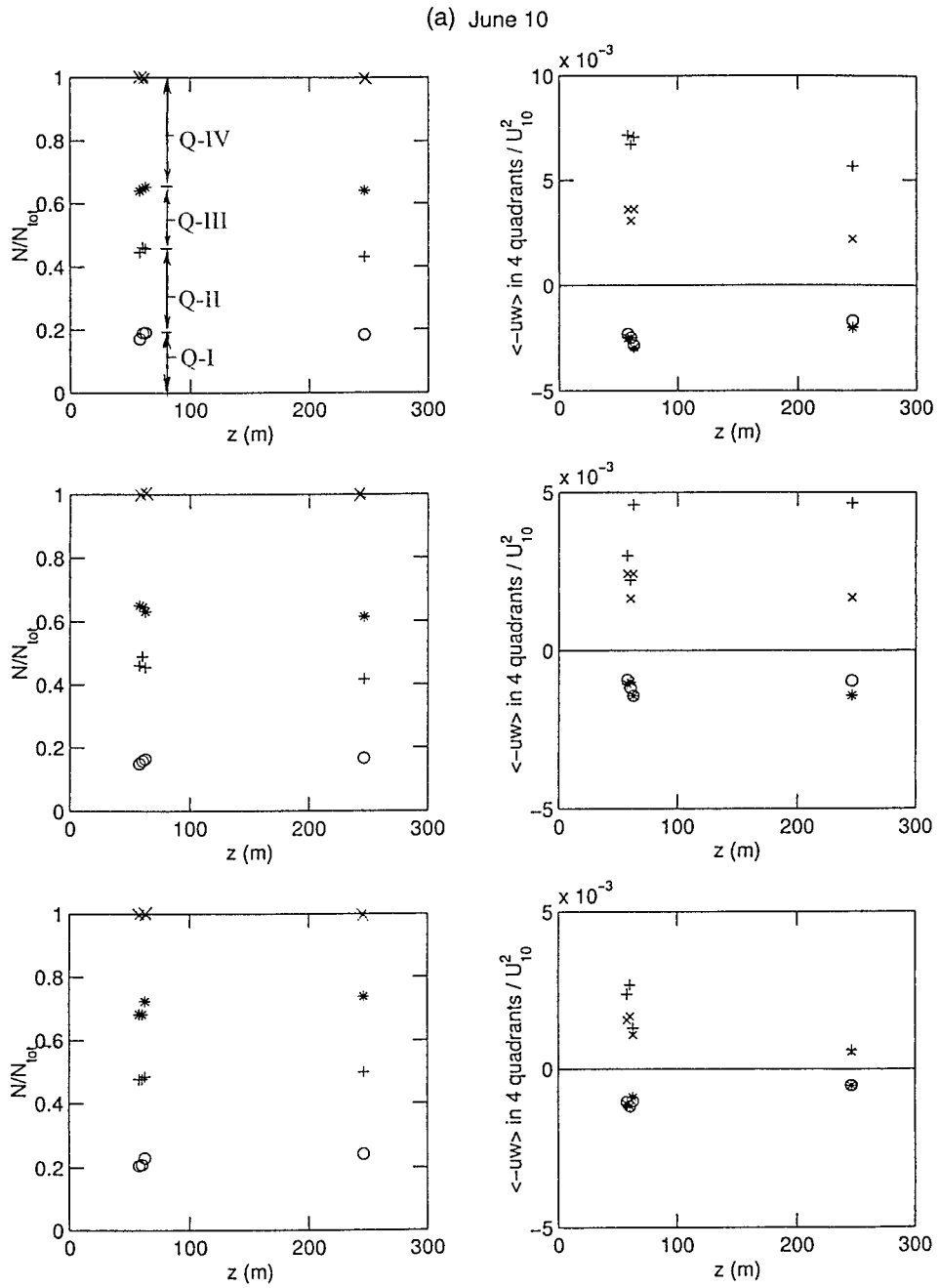

FIG. 5. Momentum flux burst statistics for (a) 10 Jun and (b) 13 Jun. (left column) The relative numbers of data points in the four quadrants N/N_{tot}, shown by the relative heights of the intervals directly *below* the indicated symbol (as indicated in the top left panel). (right column) The mean downward momentum flux contribution $\langle -uw \rangle$ from each quadrant normalized by U_{10}^2. Legend: ○ (Q-I: $u > 0$, $w > 0$); + (Q-II:

that the wavelength range of wind stress contributions is from several tens of meters to about 3 km in the crosswind direction and up to 10 km for the alongwind direction. The contribution from scales of motion less than several hundred meters is dominant at low levels, but the importance of these shorter scales decreases with height, as seen already in Figs. 4 and 5. The high $-vw$ coherence seen in Fig. 3a occurs consistently for wavelengths longer than O(500 m) at the height of 60 m and longer than O(1000 m) at the height of 246 m. According to the crosswind flight data in Fig. 6b, the momentum flux contribution from these organized roll-cell structures is about 50% of the total momentum flux at the lowest flight altitudes.

Figures 6c,d, and 6e,f show the absolute and normalized levels of the cumulative cospectra for 11 and

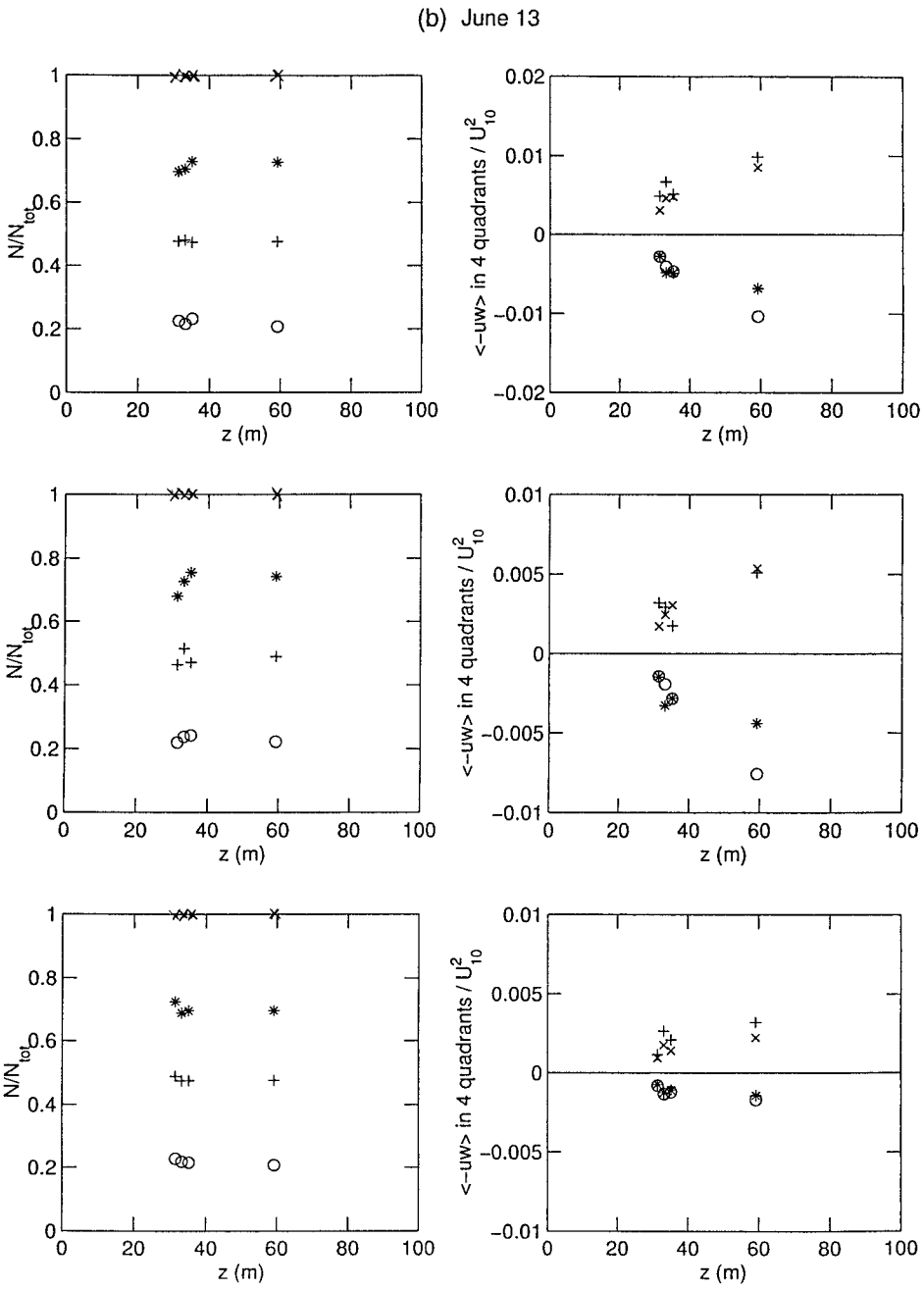

FIG. 5. (*Continued*) $u < 0$, $w > 0$); * (Q-III: $u < 0$, $w < 0$); × (Q-IV: $u > 0$, $w < 0$). The uppermost pair of figures is for the full spectral bandwidth, the center pair of figures is for wind fluctuation wavelengths longer than 300 m, and the lowest pair of figures is for wind fluctuation wavelengths shorter than 300 m.

13 June, respectively. For the moderate wind conditions on 13 June, the momentum flux gradually accumulates for wavelengths up to a few kilometers, but a large scatter of up to 50% of the total momentum flux level occurs for length scales exceeding a few kilometers. These results confirm that the presence of large-scale coherent structures can result in significant low wavenumber variations in the magnitude of the wind stress. Hence, wind stress estimates from fixed tower measurements may show considerable variability as the roll cells drift slowly across the mean flow. The lack of availability of crosswind traverse data in conjunction with fixed open ocean platform data makes it difficult to reconcile such variability.

Reference to Fig. 6 confirms that the averaging interval needed to obtain a stationary estimate of the mean momentum flux is significantly shorter for crosswind measurements than upwind/downwind measurements,

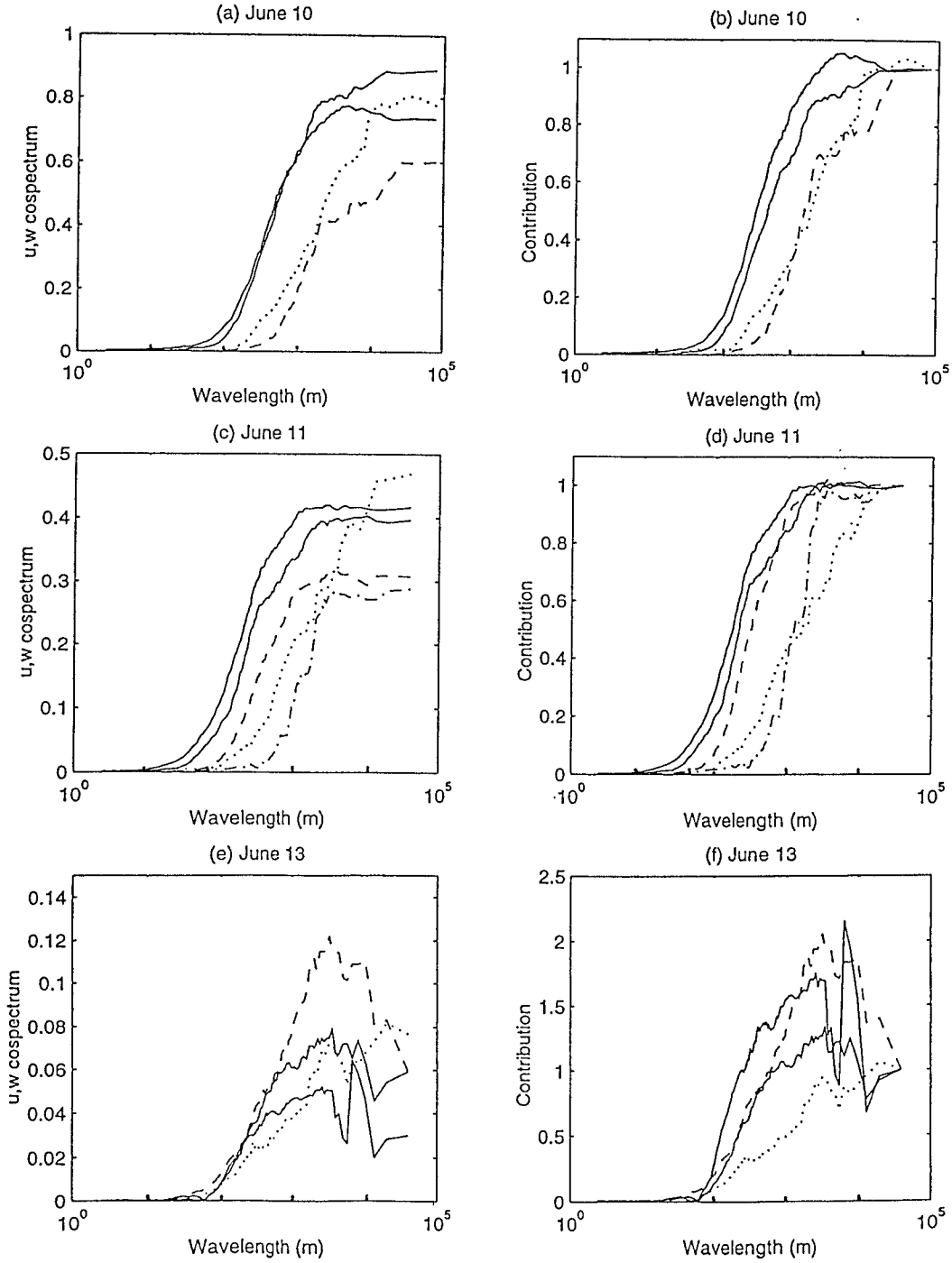

FIG. 6. Cumulative turbulent stress cospectra (ogives) for different measurement altitudes and aircraft tracks for three wind conditions ($U_{10} \approx 20$ m s^{-1} on 10 Jun, $U_{10} \approx 15$ m s^{-1} on 11 Jun, and $U_{10} \approx 9$ m s^{-1} on 13 Jun). (a) and (b) show respectively the cumulative absolute and relative stress levels (normalized by the total cospectral level integrated over all scales) from the short scales toward the longest scales for gale-force winds for 10 Jun: $z = 60$ m, c.w. tracks (solid); $z = 59$ m, u.w. track (dotted); $z = 246$ m, c.w. track (dashed). (c) and (d) As for (a) and (b) but for 11 Jun: $z = 30$ m, c.w. tracks (solid); $z = 30$ m, u.w. track (dotted); $z = 59$ m, c.w. track (dashed); $z = 246$ m, c.w. track (dot-dashed). (e) and (f) As for (a) and (b) above, but for 13 Jun: $z = 34$ m, c.w. tracks (solid); $z = 34$ m, u.w. track (dotted); $z = 59$ m, c.w. track (dashed).

that is, O(3 km) for crosswind track measurements and O(10 km) for upwind track measurements. This occurs because crosswind track measurements traverse coherent MABL structures (which are aligned generally in the streamwise direction) more frequently than alongwind measurements. We note that for a 16 m s^{-1} wind speed, a 10-km upwind traverse is comparable with a 10-min record from a fixed tower. If the coherent structures are meandering and/or skewed in the crosswind direction, much longer averaging times may be required on the tower and a stable wind stress determination may not be achieved even for longer than the customary 20-min tower averages. An example of this situation is described in section 4d.

e. Large-scale variability of the wind stress

It is of central interest in this study to examine the intrinsic variability of the wind stress as measured at the minimum aircraft heights. The wind stress determination requires averaging over sufficiently long intervals to include all scales of variation of the momentum flux components $-uw$ and $-vw$. We investigated the crosswind variation of 10-km and 20-km running averages of these momentum flux signals for two gale-force wind speed days to validate the use of 10-km crosswind averaging, based on the cumulative cospectral data shown in Fig. 6. Two representative low-level crosswind cases with reverse legs (10 and 12 June) were examined in detail. Panels a–d in Figs. 7 and 8 show, respectively, the spatial variation of the 10-km-averaged wind velocity vector, the local departure from this mean wind vector, and the 10-km and 20-km averaged momentum fluxes for these two days. Indicated in Fig. 7d and 8d are 15-km subtracks S1–S4 during one of the low-level crosswind legs. The corresponding cumulative momentum flux cospectra for these subtracks are shown in Figs. 7e and 8e.

It is seen in Figs. 7c and 7d that on 10 June, the 10-km and 20-km averaging intervals give a similar picture of the wind stress distribution, with additional smoothness apparent using 20-km averaging. There is evidence of spatial inhomogeneity in the wind stress of around $\pm 10\%$, and this is reflected in the four ogives associated with subtracks S1–S4 in Fig. 7e. On 12 June, however, Fig. 8 reveals a significant departure between the almost uniform mean wind speed distribution and the 10-km-averaged momentum flux distribution for these low-level traverses. There is an unexplained strong residual modulation in the mean momentum flux distribution in Fig. 8c, and its impact is still evident in Fig. 8d with 20-km averaging. The nonasymptotic subtrack ogives in Fig. 8e indicate that the corresponding cospectra are not closed with data records using a 15-km track length and are consistent with the highly nonstationary spatial running means of the wind stress vector seen in Figs. 8c and 8d. It is possible that this variability was caused by the interaction of clouds with the boundary layer. The unstable stratification observed during SOWEX will support cumulus clouds removing air from the boundary layer. On a few occasions (less than 3% of the total samples) there were also signatures in the temperature records to indicate the possibility of evaporating precipitation in the boundary layer.

One such example of the occurrence of precipitation is shown in Fig. 9. The bottom panel shows measurements from two temperature sensors as a function of distance along crosswind leg 3 on 12 June 1992. The standard temperature sensor is the Rosemount sensor, labeled $\mathbf{T}_{\text{rose}}$ in Fig. 9b. This sensor shows about 8°C for most of the flight leg, although between 50 and 65 km there is a marked region of colder air. Also shown is the temperature trace of another sensor, the so-called reference temperature sensor, $\mathbf{T}_{\text{ref}}$. A major difference between these sensors is that the Rosemount sensor is relatively well-shielded against liquid water contacting the sensing element, whereas the reference temperature sensor is much more exposed in its housing. As a consequence, water impinges onto the reference temperature sensor and evaporates, thus cooling the sensing element considerably. The difference between the two temperature measurements is a clear indication that the segment between 50 and 65 km was in a precipitation region. Even after the aircraft exits the precipitation region, the $\mathbf{T}_{\text{ref}}$ sensor remains partially wet for a few minutes due to the amount of water ingested into the housing. The updraft structure in the precipitation-affected region is similar to the remainder of the flight leg (see Fig. 9a), but the region does show what appears to be a divergent pattern in the northwestern part of crosswind leg 3 (c.w.3 in Fig. 8b). It is possible that much of the large-scale (>10 km) variation in horizontal wind velocity in this and other flight legs is due to the interaction between the boundary layer and clouds above, but a mapping of the cloud fields was not done during SOWEX. In any event, this serves to highlight one of the potential factors contributing to the apparent lack of a universal averaging interval for determining the wind stress.

3. Coupling of seasurface roughness and atmospheric motion variability

a. The mean square slope as a sea surface roughness measure

Wind waves occur on the sea surface with wavelengths ranging from a few millimeters up to several hundred meters. Although larger-scale waves contain most of the wave energy, small-scale wavelets that make up the sea surface microstructure are known to play an important role in interfacial transfer processes. These small-scale waves transfer the momentum they absorb from the wind to larger gravity waves and surface-layer currents through nonlinear wave–wave interactions and microscale wave breaking. The importance of micro-

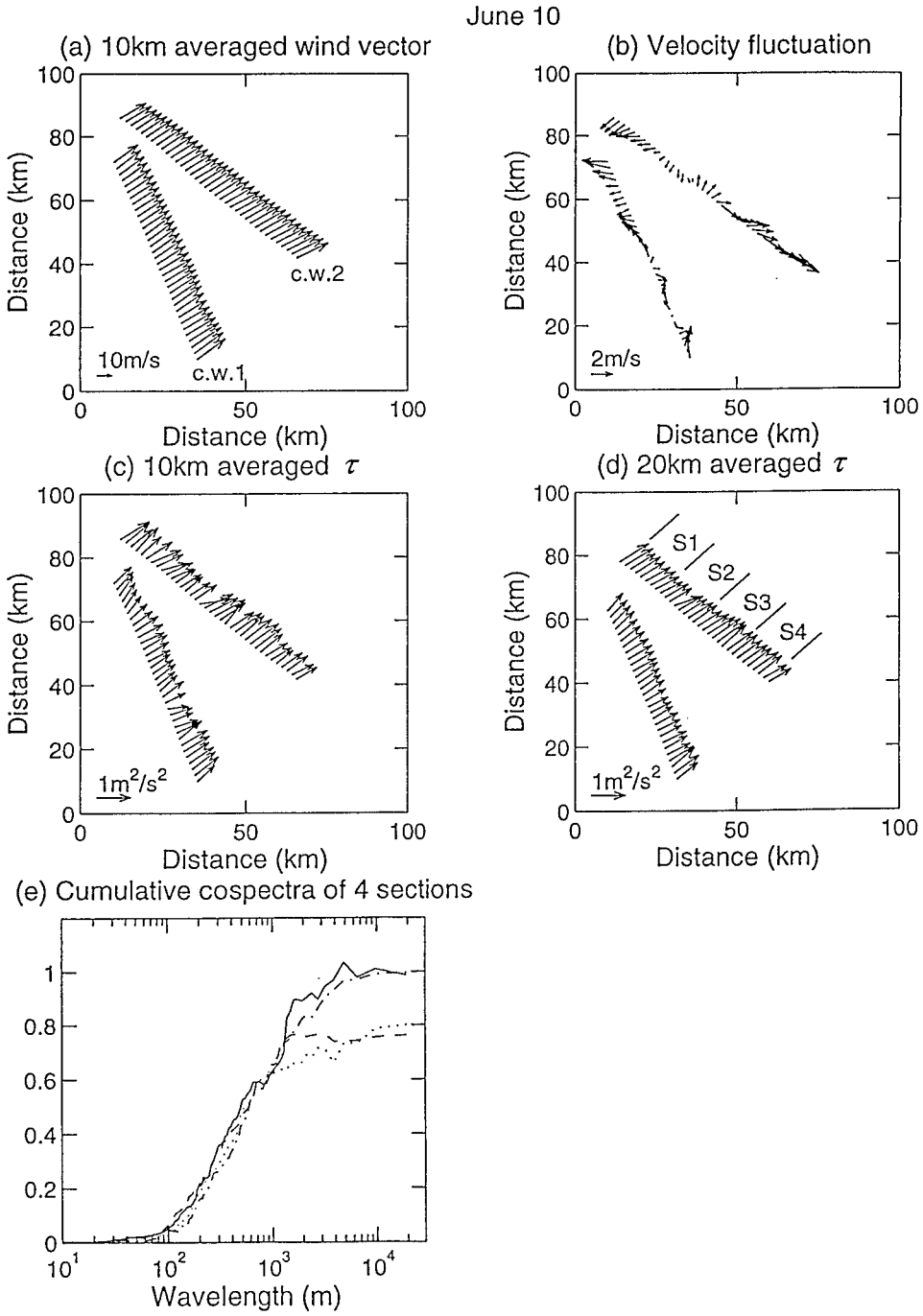

FIG. 7. The low-level cross-track variation during the gale-force wind conditions on 10 Jun of (a) the mean wind speed (averaged over 10 km), (b) the local departure from the mean wind velocity, (c) the 10-km-averaged momentum flux vector, and (d) the 20-km-averaged momentum flux vector. (e) The cumulative stress cospectra averaged over 15 km for the indicated subtracks S1 (solid), S2 (dashed), S3 (dot-dashed), and S4 (dotted) in (d).

scale breaking in the air–sea interaction momentum transfer process lies in the associated onset of local airflow separation over these wavelets, which nearly doubles their local aerodynamic form drag (Banner 1990). Thus, despite their small physical dimensions, the ubiquity of microscale breaking waves on the sea surface warrants their inclusion as an important contributor to the sea surface roughness. The sea-surface mean square slope (mss) is weighted to shorter scales and includes these small-scale breakers. Further, we recall that Plant

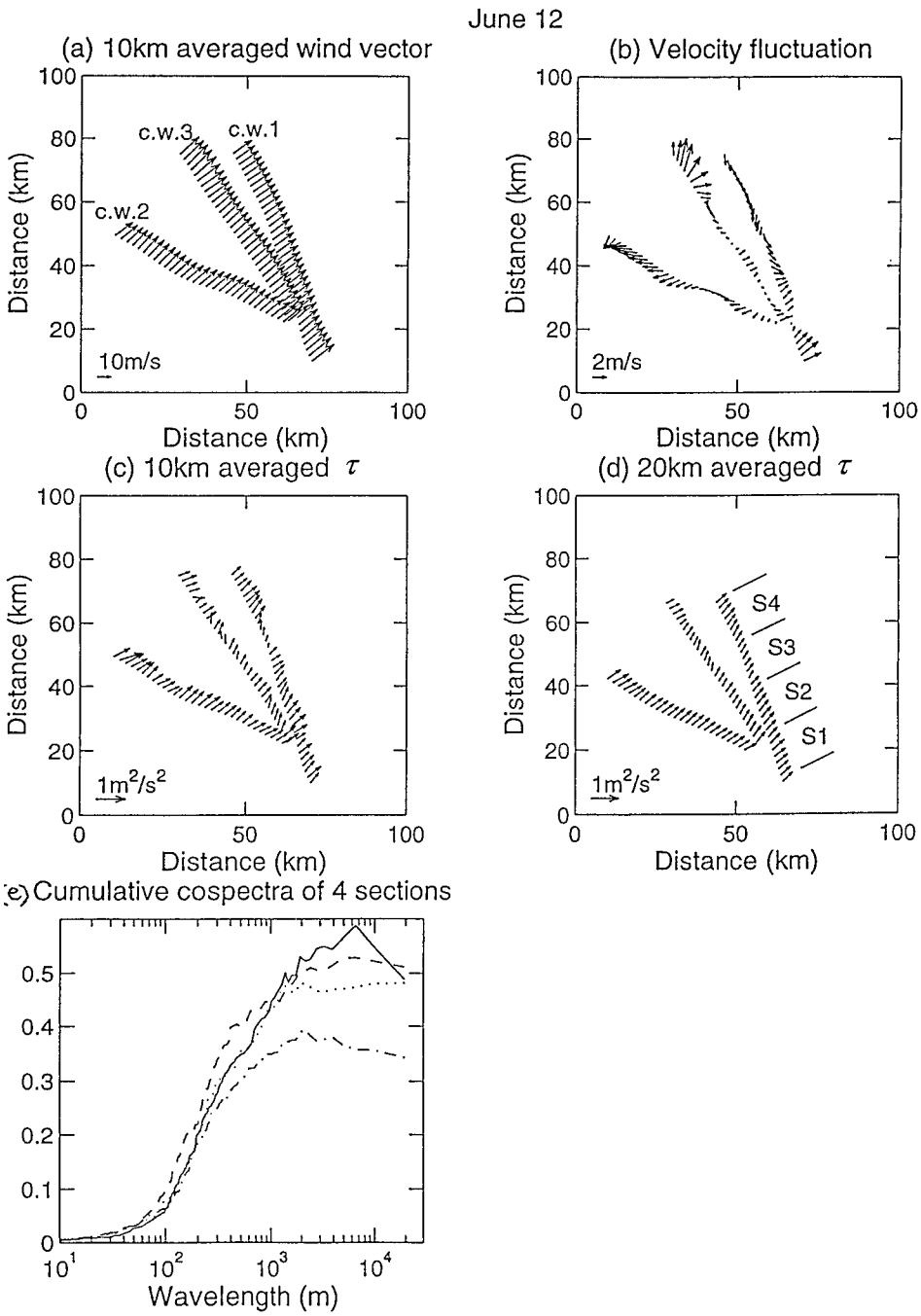

FIG. 8. The low-level crosswind variation during the gale-force wind conditions on 12 Jun of (a) the mean wind speed (averaged over 10 km), (b) the local departure from the mean wind velocity, (c) the 10-km-averaged momentum flux vector, and (d) the 20-km-averaged momentum flux vector. (e) The cumulative stress cospectra averaged over 15 km for the indicated subtracks S1 (solid), S2 (dashed), S3 (dot-dashed), and S4 (dotted) in (d).

(1982) linked the level of wave-induced drag directly to mss, which therefore represents a closer connection to the air–sea interaction dynamics than does the wave height. These issues have been discussed in detail in section 1 of S1.

Measurement of small-scale waves presents an observational challenge because conventional wave-data instruments such as wave-rider buoys are only able to resolve larger-scale waves. The classic Cox and Munk (1954) study overcame this by using optical roughness properties of the sea surface based on sun glint measurements. This technique involves the slopes of wave

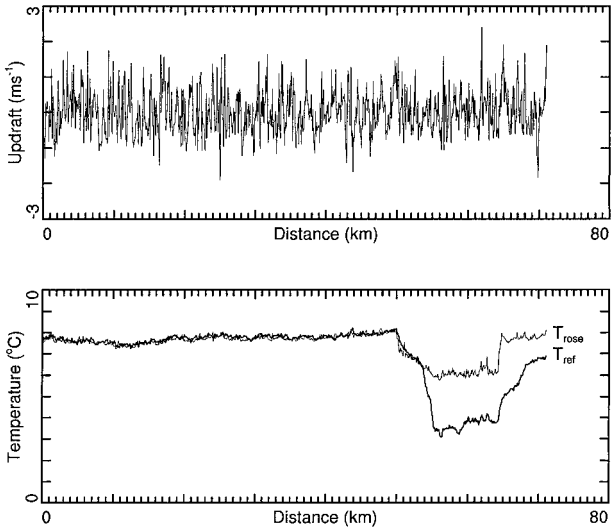

FIG. 9. Vertical velocity (w) and temperature (T) for crosswind 3 leg on 12 Jun 1992. The distance scale begins in the southeast end of the flight leg. The temperatures are for two different sensors, the Rosemount sensor ($\mathbf{T}_{rose}$) and the ''reference'' sensor ($\mathbf{T}_{ref}$). The marked difference between them is in a region identified as affected by precipitation droplets.

components on all scales and includes the contributions from the sea surface microstructure down to the smallest capillary waves. In SOWEX we deployed the 36-GHz NASA Scanning Radar Altimeter (SRA) to measure the directional components of the mss. This technique resolved wavelengths down to about 20 mm, but required averaging over 1.9 km for statistically reliable averages. It also resolved the underlying large-scale wave height topography simultaneously with the surface layer wind turbulence data, in both alongwind and crosswind directions.

A detailed discussion of the SRA data-extraction methodology is given in S1, to which the interested reader is referred. In S1, we also reported the observed variation of large-scale average mss with wind speed up to $U_{10} \approx 20$ m s^{-1} during SOWEX. An additional consideration not described in S1 was required to measure the local variability of the mss and involves the minimum number of scan lines of SRA power data needed to extract a stable local mss estimate. The minimum number was determined to be 256 scan lines, which translates into the 1.9-km averaging distance quoted in the previous paragraph, based on an aircraft speed of 76 m s^{-1} and the 10-Hz SRA scan rate. Below, we report our key findings on the local variability of the mss in response to local wind speed variations, as well as the behavior of allied quantities of interest such as the off-nadir radar backscatter. We also discuss the implications of these observations for interpreting the SAR image striations shown in Fig. 1, for wind scatterometer response and for the form of the high wavenumber sea-surface spectrum.

b. Mean square slope variations

Historically, finding a strong correlation between wind variables and sea state variables from local measurements has proven to be elusive. Using slant range data from different wavenumber band radars observed from an open ocean platform, Weissman et al. (1994) reported that the variations of backscattered power of X-band and K_a-band radars were correlated with wind speed variations, but only for averages over time intervals exceeding 2 minutes.

From our measurements of simultaneous atmospheric and SRA data, we were able to compare the variations of the sea state with the corresponding variations of the wind speed and momentum flux. Figures 10a–c show these results for representative crosswind and upwind measurements during moderate and strong wind conditions. The mss shown in these figures was averaged over each set of 256 scan lines (1.9 km) of SRA data along the track. The root-mean-square wave height, which represents the variation of the wave energy, was also computed over the same averaging distance of 1.9 km (about 15 dominant ocean wavelengths) and also over twice this distance (3.8 km). The backscattered radar power measured at oblique incidence angles is believed to be associated with resonant Bragg scattering and is proportional to the sea surface roughness (see Robinson 1985). The SRA nominally scans out to 22° off-nadir, but the sea surface tilt and varying aircraft roll attitude increase the range of local incidence angles. For Figs. 10a–c we averaged the backscattered power for local incidence angles larger than 15° to weight the reflected power toward Bragg scattering, although a specular contribution could still be present. We used a 1.9-km averaging distance for the sea surface roughness data and the wind speed data. As discussed in the previous section, we retained the minimum 10-km averaging distance for the momentum flux measurements shown in these figures. At the 95% confidence level, our estimates for the standard error of the mean are 0.09 m s^{-1}, 0.043 m^2 s^{-2}, and 0.004 for the mean wind speed, momentum, flux, and mss. This uncertainty is significantly less than the instrumentation errors, which are summarized in the appendix.

Figures 10a–c reveal a number of interesting features. For both strong and moderate wind conditions, the variations of mss and backscattered power with larger than 15° incidence angles correlate strongly with the wind speed. In particular, the fractional variations of these quantities shown in the lowest plots agree closely with those of the wind speed. It is also seen that the variations of the 10-km-averaged momentum flux at the aircraft height and mss show much lower visual correlation than the correlation between variations in wind speed and mss.

At first sight, the observed linear wind speed dependence of mss and off-nadir backscattered power might be surprising in view of the quadratic wind speed de-

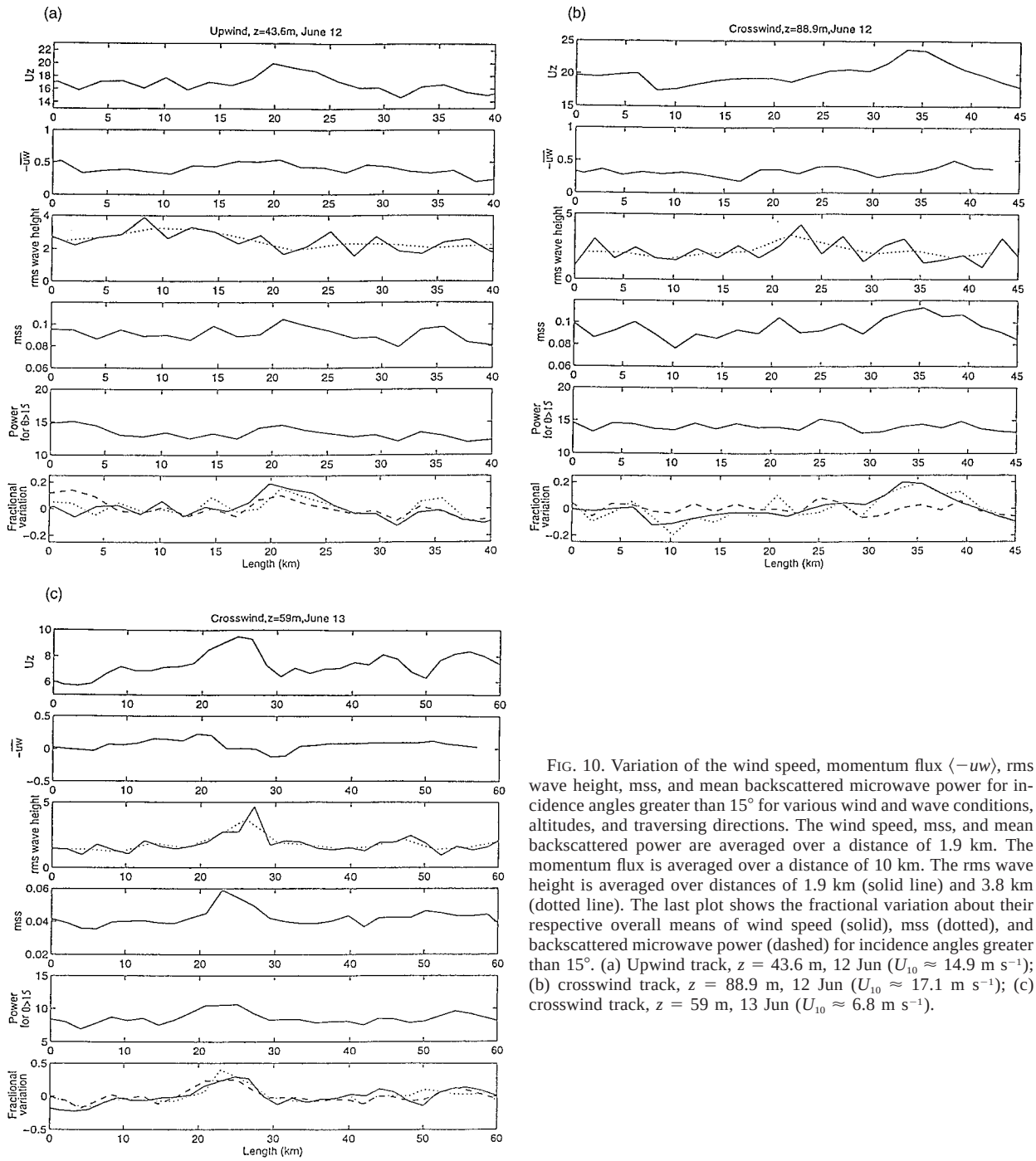

FIG. 10. Variation of the wind speed, momentum flux $\langle -uw \rangle$, rms wave height, mss, and mean backscattered microwave power for incidence angles greater than 15° for various wind and wave conditions, altitudes, and traversing directions. The wind speed, mss, and mean backscattered power are averaged over a distance of 1.9 km. The momentum flux is averaged over a distance of 10 km. The rms wave height is averaged over distances of 1.9 km (solid line) and 3.8 km (dotted line). The last plot shows the fractional variation about their respective overall means of wind speed (solid), mss (dotted), and backscattered microwave power (dashed) for incidence angles greater than 15°. (a) Upwind track, $z = 43.6$ m, 12 Jun ($U_{10} \approx 14.9$ m s^{-1}); (b) crosswind track, $z = 88.9$ m, 12 Jun ($U_{10} \approx 17.1$ m s^{-1}); (c) crosswind track, $z = 59$ m, 13 Jun ($U_{10} \approx 6.8$ m s^{-1}).

pendence of the wind input source function. In this regard, it is noted that wind wave growth is not due to the wind input alone, but is the net result of the nonlinear wave–wave interactions and wave dissipation in conjunction with the momentum transfer from the wind. It is important to note that it is not possible to relate *local* mss variability to wind stress variations. This is due to the intrinsically larger spatial averaging distances required to determine the wind stress.

The SOWEX mss results are consistent with the linear wind speed dependence of mss over a larger spatial scale, as reported by Cox and Munk (1954). Aside from our reservation on the use of the wind stress as the local measure of wind forcing, these results are also consistent

with the recent findings of Hwang et al. (1996) that the spectral level of short ocean waves (wavelengths between 4 and 60 mm) has a linear dependence on the atmospheric friction velocity. After integration over the spectrum, however, spectral dependences on wind speed other than linear can produce an overall linear wind speed dependence for the mss. Therefore, our mss measurements do not provide a direct validation of the Hwang et al. (1996) findings and further measurements of the wind speed dependence of the short wind wave spectrum are needed to confirm these findings.

These figures also show that rms wave height variations are not well correlated with variations in wind speed or wind stress. This is not unexpected since the rms wave height is dominated by the larger scale waves that are only weakly coupled to the local wind for these mature wind seas and swells.

These spatial distributions further confirm the influence of large-scale atmospheric motions on the surface-layer momentum flux distribution based on 10-km averaging. According to present understanding, the increased surface wind speed and sea surface roughness observed over O(10 km) regions should result in an increased wave drag and total drag. Yet the measurements show that these regions of increased surface wind speed and roughness are not necessarily accompanied by a proportional increase in the momentum flux observed at 40 m or higher. Given the complex interaction between large-scale roll-cell structures and the sea surface, the strength of possible horizontal divergence of the momentum flux closer to the surface is unresolved by our data. This aspect needs to be further refined to improve modeling of the near-surface wind field during such unstable conditions.

c. Mean distribution of mss over the dominant waves

From our measurements of mss and mean backscattered power within $\pm 5°$ of nadir over different locations along the dominant wave profile, we were able to determine the distribution of small-scale wave roughness riding on the large-scale waves. This analysis made use of a 45-km data segment measured during an upwind track, which included about 160 dominant waves. We binned the radar power returns from within the same surface elevation range (using 0.5-m bins) and the same surface tilt range (using 0.01-rad bins), obtaining the variations of mss and mean backscattered nadir-look power with surface elevation and surface tilt shown in Figs. 11a and 11b. The lower plot in each of these figures is the histogram of the sample sizes in each elevation or tilt bin.

The increasing trend of the mss and decreasing trend of the mean backscattered nadir-look power with surface elevation seen in Fig. 11a indicate that the sea surface roughness increases slowly with the surface elevation. Thus, on the average, for these wind and wave conditions typical of mature wind seas, the dominant wave

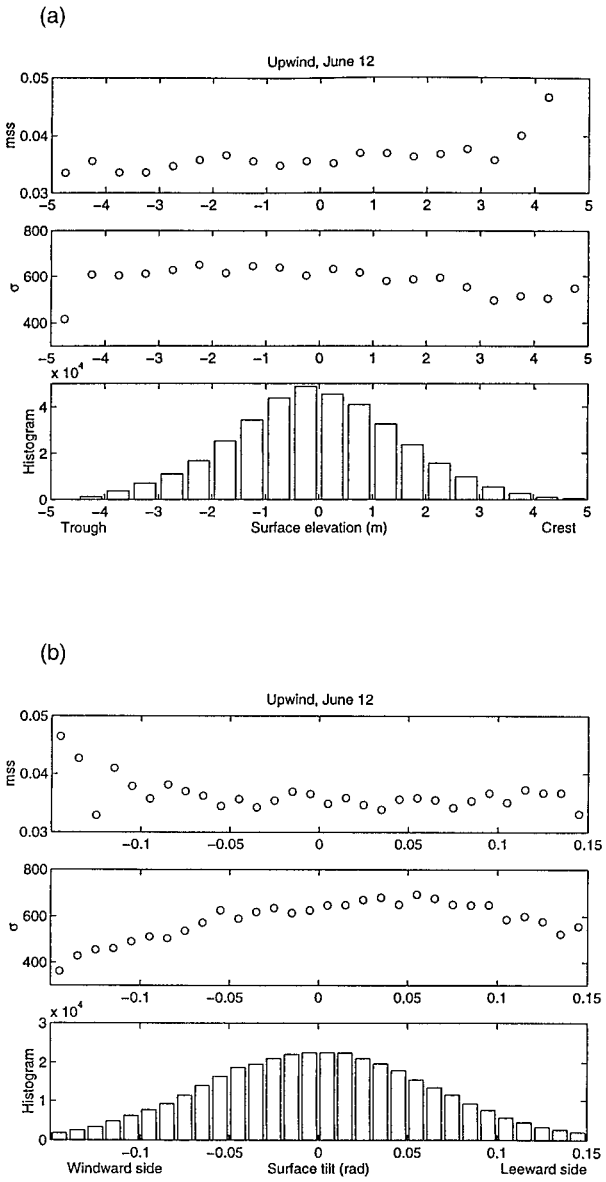

FIG. 11. (a) Variation of binned mss and backscattered microwave power σ (in arbitrary units) near nadir with respect to the binned surface elevation, calculated over about 160 dominant waves, showing that the dominant wave crests are statistically rougher than the troughs. (bottom) The histogram of the data points in the ensemble. (b) Variation of binned mss and backscattered microwave power near nadir with respect to the binned surface tilt, calculated over about 160 dominant waves, showing that the windward face is statistically rougher than the leeward face of the dominant waves. (bottom) The histogram of the data points in the ensemble.

crest regions are statistically rougher than the trough regions. This roughness variation causes the so-called electromagnetic bias of the sea surface, which is known to influence the accuracy of satellite altimeters. Their measurements of mean sea level are biased negatively by a few percent of the sea wave height due to this differential local radar reflectivity of troughs and crests

of the dominant waves. A complementary aspect of SOWEX discussed by Hevizi et al. (1993) determined the electromagnetic bias for high sea state (9-m significant wave height) conditions as part of the development of the correction algorithm for the NASA altimeter on the TOPEX/Poseidon satellite.

Another interesting wave surface characteristic available from these measurements is the relative roughness of the windward and leeward faces of the dominant waves. The observed decreasing trend of the mss and increasing trend of the mean backscattered power with surface tilt are shown in Fig. 11b. These trends indicate that the windward side of waves, identified by negative surface tilt values, is rougher on average than the leeward side of waves, identified by positive surface tilt values.

4. Discussion

a. Coherent structures

During SOWEX, phase-coherence spectral analysis of the velocity field revealed that large-scale atmospheric roll cells dominated the MABL flow at appreciable (246 m) heights above the sea surface. Similar analysis of the low-level flight data indicated that coherent structures continued to make a significant contribution to the downward momentum flux much closer to the sea surface, but our results indicate that the transverse length scale of these coherent structures extended down to about 400 m. This important finding is consistent with our intermittency results in section 2c and is discussed more fully in the following paragraph. The relationship of these coherent structures to the streamwise striations visible in the SAR imagery in Fig. 1 is also addressed in the subsection below.

For the large fetches involved, within a few tens of meters of the sea surface, it was anticipated that boundary-generated turbulence would dominate the air–sea momentum flux. Our results, however, show that at these very low altitudes, the momentum flux cospectrum still received significant contributions from roll-cell structures with transverse wavenumbers ranging over the significant range of length scales from 400 to 1000 m. The basis for this conclusion is our phase-coherence data for the v and w components at the lowest aircraft heights during the crosswind flight legs in Fig. 3, which show close to the $\pm 90^\circ$ phase signature that identifies roll-cell structure. It is possible that the shorter wavelengths in this spectral subrange are manifestations of the second class of elongated ''inactive eddies'' discussed by Mourad (1996). Further analysis of our data is being undertaken using localized spectral analysis techniques and this may clarify the physical mechanisms involved. In any event, reference to the associated velocity cospectra in Fig. 4 confirms that the momentum flux contribution of these scales is significant.

It is interesting to note that the *uw* phase data show $\pm 180^\circ$ shifts over a considerably wider spectral range, but after investigation, we believe that this *uw* phase signature alone is unable to confirm conclusively the presence of roll-cell structures. Antonia and Chambers (1980) reported similar $\pm 180^\circ$ phase shifts in their tower-based measurements of *uw* cospectra from the lowest frequencies to just below the spectral peak frequency. While their 5-m elevation observations were made for weakly unstable atmospheric conditions during mature windseas and wind speeds below 9 m s^{-1}, they were unable to determine whether roll cells were present or not. R. A. Antonia (1998, personal communication) also found very similar *uw* phase relationships for wind tunnel rough wall turbulent boundary layers. Again, no crosswind traverse data were available to confirm the possible presence of coherent lateral structures corresponding to the extensive spectral range of *uw* phase-coherence data showing $\pm 180^\circ$ phase shifts. A literature search of the MABL roll-cell observations suggests that this significant aspect of available crosswind track data has not been routinely reported, hence it is very desirable that our conclusions on the spectral bandwidth of coherent roll-cell structures should be confirmed in existing and future datasets.

Our sampling of the wind field does not provide an immediate explanation for these unanticipated findings. The fluid dynamical processes underlying the coherent structural properties of the velocity field in the marine boundary layer that we observed throughout SOWEX clearly require further investigation. This appears to be of fundamental importance in correctly modeling the dynamical behavior of the MABL in the typically unstable open ocean conditions encountered during SOWEX.

b. Large-scale variability

We investigated the large-scale spatial variability of the average momentum flux to the sea surface (at the observation height) over distances O(80 km). Here, we observed cases where the mean momentum flux, averaged either over 10 km or 20 km, was reasonably spatially uniform. We also observed a case where the wind field was close to uniform, but the average momentum flux showed very strong large-scale variability across the flow, on scales O(20 km), which is much larger than typical large-scale roll-cell wavelengths. Etling and Brown (1993, sec. 3.4) discuss a number of possible mechanisms that might be responsible for the observed large aspect ratios, but our limited sampling of this effect provides us with no conclusive explanation for these larger-scale modulations. One possibility suggested in section 2c is an interaction between the MABL and the overlying clouds. Further clarification of the large-scale variability in the wind stress is left for future investigation.

c. Surface roughness striations

Dark surface striations are often observed in SAR images as cells with O(1 km) spacings aligned closely with the wind direction (Fig. 1). They appear to be associated with the surface flow field of atmospheric roll cells. These darkened streaks have reduced microwave reflectivity and are therefore areas of decreased mss and reduced mean wind speed. This follows from the very strong correlation we found (see below) between wind speed variations and mss variations on scales longer than the 1.9-km averaging distances needed for stable mss determinations. According to the generic roll-cell flow structure shown in Fig. 2, the low wind speed striations correspond to coherent updraft zones and therefore correspond to regions of enhanced momentum flux to the sea surface (as determined at the aircraft height) since their $\langle -uw \rangle$ contribution is systematically positive.

We were unable to resolve mss variations on scales O(1 km), hence we could not show directly that roll-cell updraft zones coincided with the striations. The supporting evidence is therefore indirect and certain aspects remain unresolved. Our spectral data (Fig. 4) confirm that the momentum flux cospectrum level for these scales was still significant in our lowest level measurements. To be consistent with the inferred reduction in short-wave energy levels observed in the striations, the locally reduced downward momentum flux in the updraft zones at the surface needs to couple with locally enhanced downward momentum flux in the updraft zones at greater altitudes. We speculate that there must be considerable stress divergence within the surface layer for this to occur. Our data do not provide sufficient information to evaluate this intriguing behavior and this aspect of the observations remains to be addressed in future studies.

d. Wind parameterization in the wave height spectrum

Depending on the scale of interest, the atmospheric friction velocity u_* may be inappropriate as the wind parameter in the spectral description of the short waves. The wind stress inherently requires an averaging interval that exceeds the observed roll-cell scale and hence cannot in principle describe the observed short-wave roughness variations O(1 km) scales such as are seen in Fig. 1. Even over larger spatial scales, our results show that the local response of the short waves is more closely correlated with the local mean wind velocity than with the atmospheric friction velocity. Therefore, the wind speed is the preferred wind parameter if local short-wave variability features are to be reliably resolved by the wave spectral model.

As a related issue, available evidence from laboratory wind wave observations (e.g., Jähne and Riemer 1990) and ocean radar backscatter data (e.g., Jones and Schroeder 1978) suggests that the wind speed sensitivity of short gravity–capillary waves increases as their wavenumber increases. In seeking a parameterization for the wind dependence of the wave-height wavenumber spectrum, the choice of spectral dependence of the wind exponent is of central importance and affects the reliability of subsequent modeling predictions. Thus, while the explicit wind speed exponent of the high wavenumber spectral tail was not resolved by our measurements, our mss results with O(20 mm) resolution provide unique data for validating such wavenumber spectral models for mature open-ocean conditions and wind speeds up to $U_{10} \approx 20$ m s^{-1}. Any model should reproduce the observed mss levels and overall linear dependence with wind speed in both downwind and crosswind directions, as reported in Fig. 13 in SI and confirmed here in the observed local variability of the mss, as shown in the lowest panels of Figs. 10a–c.

Our data also contribute to the technologically important area of wind scatterometer response. A long-standing basic question has been whether the scatterometer actually measures wind speed or wind stress. Our off-nadir radar backscatter data at 36 Ghz for the limited range of incidence angles available from the SRA is also seen in the lowest panels of Figs. 10a–c to closely follow the local sea surface roughness variations and wind speed variations, implying that the scatterometer should be able to report reliable mean near-surface wind speed estimates when averaged over its typical O(50 km) spatial footprint for wind speeds U_{10} up to at least 20 m s^{-1}. As to whether the scatterometer accurately reports the wind stress, we sometimes observed large variability in the 20-km-averaged momentum flux, hence the further assumption is required that averaging over a much larger-scale area will lead to a stable drag coefficient relationship. While it seems reasonable to expect this, a direct confirmation was beyond the scope of the present study.

5. Conclusions

The SOWEX dataset has provided the first spatially extensive measurements of ocean surface layer wind velocity, momentum flux, and collocated sea surface roughness [wave height and mss (averaged over 1.9 km)] for gale-force wind conditions (up to 20 m s^{-1}) and severe sea states (up to 9.2 m SWH). The data were collected from a research aircraft using O(80 km) flight tracks, both crosswind and in the upwind/downwind direction during the weakly unstable atmospheric stability conditions that prevailed.

The atmospheric wind field structure was dominated by large-scale roll cells with dimensions typically the height of the MABL. These roll cells dominated the momentum flux well above the sea surface. Our analysis also indicated the presence of a spectral subrange of large-scale roll cells contributing to the downward momentum flux even at the lowest heights (30–60 m) above

the sea surface that could be safely negotiated in the aircraft. We believe that this unexpected finding is consistent with the presence of longitudinal striations observed in SAR imagery, such as shown in Fig. 1 and reported by other investigators (e.g., Alpers and Brummer 1994; Mourad 1996).

The darkened sea surface streaks that are seen in the SAR imagery are associated with reduced wind speed and lower short wind wave energy levels (and mss), and should correspond to updraft zones of roll cells. Consistent with this interpretation, the dark striations should have locally reduced momentum flux levels. On the other hand, far above the sea surface, updraft regions of roll cells have been identified as sites of locally enhanced downward momentum flux. It therefore remains to be understood how, with increasing altitude, the momentum flux transitions within these updraft regions from locally reduced to locally enhanced. Due to their inherent 1.9-km averaging distance requirements, the present mss measurements do not resolve this intriguing effect, which appears to be associated with a complex stress divergence pattern. This clearly warrants further investigation, possibly in terms of the multiscale structure interpretation of Mourad (1996) and appears to be closely related to the issue raised previously in section 2d concerning the relative strength of momentum fluxes at the sea surface associated with roll cells and surface-generated turbulence.

On a larger scale, we observed occasional examples of crosswind variations in the magnitude and direction of the wind stress over 20-km length scales. We believe that this inhomogeneity may have been associated with the flow induced by local precipitation shafts. When these inhomogeneities occur, our data suggest that they can contribute significantly to the large-scale variability observed in drag coefficient measurements.

One of the primary aims underlying SOWEX was to determine to what extent sea surface roughness followed variations in the wind field, particularly during very strong wind conditions. Our intercomparison of each of the variables measured in SOWEX shows that variations in wind speed and mean square slope stood out as the two variables that were most strongly correlated, with close to a linear dependence. This confirms locally the results that Cox and Munk (1954) obtained using much larger-scale averaging and also extends their applicable wind speed range from $U_{10} \approx 14$ m s^{-1} up to 20 m s^{-1} (SI).

In contrast, the wind stress and the wave height showed far lower visual correlation with wind speed variations. We found that the long averaging intervals needed for stable estimates of the wind stress render it, or equivalently the friction velocity u_*, a very nonlocal measure. It appears to be intrinsically unsuitable as a parameter to describe the observable coherent variations in sea surface roughness on 1-km scales, such as those commonly seen in SAR images representing the surface signature of atmospheric roll cells. Our results show that local wind speed gives a superior indication of local roughness variations and should be considered as the preferred wind parameter in wavenumber spectral models if such local variations are to be resolved. The friction velocity is then more appropriate for parameterization of average wind forcing on much larger scales, such as those typically sampled by the scatterometer.

Our findings on the behavior of the mss also have significant implications for the wave-height wavenumber spectrum for mature sea states. From our results, the integrated effect of the wind speed or friction velocity dependence for scales down to 2-cm wavelengths should result in an overall linear wind speed variation for U_{10} up to 20 m s^{-1} for well-developed seas. This provides a valuable integral constraint on any proposed wind speed dependence in the representation of the wave spectrum.

Acknowledgments. The authors gratefully acknowledge the support provided for this project by the Australian Research Council, the National Science Foundation (U.S.A.), and the CSIRO Division of Marine Research.

APPENDIX

Brief Summary of Instrumentation and Accuracy Issues

Instrumentation on the F27 was laboratory-calibrated for SOWEX. Additional in-flight maneuvers were necessary in order to account for aircraft-induced changes to flow angles, temperature, and pressure measurements. This was accomplished by tower fly-bys and by conducting reverse heading legs, speed runs, Dutch roll, and roller-coaster procedures as described by Lenschow (1986). These in-flight maneuvers assume smooth air along the flight tracks and were carried out above the boundary layer. Circular flights were also used to check the measurements. In practice there are several causes of mean velocity measurement uncertainty, including nonsteady airflow and inertial navigation system (INS) drift. The implication is that short-term mean wind speed errors may be of order 0.3 m s^{-1}, but that these may increase for longer time averages due to the INS drift. The average vertical velocity measurement is expected to be accurate to less than a few tenths of a meter per second. For the fluctuating velocities, we estimated the overall accuracy of the wind stress measurements (including calibration and sampling variability) to be better than $\pm 10\%$. The uncertainty in the 1.9-km-averaged mss estimates was determined as $\pm 3\%$ (Chen 1997, Fig. 4.12). Wind data were logged at 64 Hz, but measurements at rates higher than 12 Hz (approximately 0.1 cycles s^{-1}) were affected by vibration of the nose boom.

REFERENCES

Alpers, W., and B. Brummer, 1994: Atmospheric boundary-layer rolls observed by the synthetic aperture radar aboard the *ERS-1* satellite. *J. Geophys. Res.*, **99,** 12 613–12 621.

Antonia, R. A., and A. J. Chambers, 1980: Wind-wave induced disturbances in the marine boundary layer. *J. Phys. Oceanogr.*, **10,** 611–622.

Banner, M. L., 1990: The influence of wave breaking on the surface pressure distribution in wind-wave interactions. *J. Fluid Mech.*, **211,** 463–495.

——, W. Chen, E. J. Walsh, J. Jensen, S. Lee, and C. B. Fandry, 1999: The Southern Ocean Waves Experiment. Part I: Overview and mean results. *J. Phys. Oceanogr.*, **29,** 2130–2145.

Boyle, P. J., K. L. Davidson, and D. E. Spiel, 1987: Characteristics of over-water surface stress during STREX. *Dyn. Atmos. Oceans*, **10,** 343–358.

Brown, R. A., 1980: Longitudinal instabilities and secondary flows in the planetary boundary layer: A review. *Rev. Geophys. Space Phys.*, **18,** 683–697.

Brummer, B., 1985: Structure, dynamics and energetics of boundary-layer rolls from KonTur aircraft observations. *Beitr. Phys. Atmos.*, **58,** 237–254.

Chen, W., 1997: An observational study of the variability of the wind stress and sea-surface roughness. Ph.D. dissertation, The University of New South Wales, 94 pp.

Cox, C., and W. Munk, 1954: Statistics of the sea surface derived from sun glitter. *J. Mar. Res.*, **13,** 198–227.

Donelan, M. A., 1990: Air–sea interaction. *The Sea.* Vol. 9: *Ocean Engineering Science*, B. LeMehaute and D. M. Hanes, Eds., Wiley-Interscience, 239–292.

Etling, E., and R. A. Brown, 1993: Roll vortices in the planetary boundary layer: A review. *Bound.-Layer Meteor.*, **65,** 215–248.

Friehe, C. A., and Coauthors, 1991: Air–sea fluxes and surface layer turbulence around a sea-surface temperature front. *J. Geophys. Res.*, **96,** 8593–8609.

Fu, L., and B. Holt, 1982: Seasat views oceans and sea ice with synthetic aperture radar. Jet Propulsion Lab Publ. JPL 81-120, Pasadena, CA, 200 pp.

Gerling, T. W., 1986: Structure of the surface wind field from the Seasat SAR. *J. Geophys. Res.*, **91,** 308–320

Glendening, J. W., 1994: Flux variations created by roll vortices over the ocean. Preprints, *Second Int. Conf. on Air–Sea Interaction and Meteorology and Oceanography of the Coastal Zone*, Lisbon, Portugal, Amer. Meteor. Soc., 50–51.

Hein, P. F., and R. A. Brown, 1988: Observations of longitudinal roll vortices during artic cold air outbreaks over open water. *Bound.-Layer Meteor.*, **45,** 177–199.

Hevizi, L. G., E. J. Walsh, R. M. McIntosh, D. Vandemark, D. E. Hines, R. N. Swift, and J. F. Scott, 1993: Electromagnetic bias in sea-surface range measurements at frequencies of the TOPEX/Poseidon satellite. *IEEE Trans. Geosci. Remote Sens.*, **31,** 376–388.

Hwang, P. A., S. Atakturk, M. A. Sletten, and D. B. Trizna, 1996: A study of the wavenumber spectra of short water waves in the ocean. *J. Phys. Oceanogr.*, **26,** 1266–1285.

Jähne, B., and K. S. Riemer, 1990: Two-dimensional wave number spectra of small-scale water surface waves. *J. Geophys. Res.*, **95C,** 11 531–11 546.

Jones, W. L., and L. C. Schroeder, 1978: Radar backscatter from the ocean: Dependence on surface friction velocity. *Bound.-Layer Meteor.*, **13,** 133–149.

LeMone, M. A., 1973: The structure and dynamics of horizontal roll vortices in the planetary boundary layer. *J. Atmos. Sci.*, **30,** 1077–1091.

——, 1976: Modulation of turbulence energy by longitudinal rolls in an unstable planetary boundary layer. *J. Atmos. Sci.*, **33,** 1308–1320.

Lenschow, D. H., 1986: Aircraft measurements in the boundary layer. *Probing the Atmospheric Boundary Layer*. D. H. Lenschow, Ed., Amer. Meteor. Soc., 39–55.

Mourad, P. D., 1996: Inferring multiscale structure in atmospheric turbulence using satellite-based synthetic aperture radar imagery. *J. Geophys. Res.*, **101** (C8), 18 433–18 449.

——, and B. A. Walter, 1996: Viewing a cold air outbreak using satellite-based synthetic aperture radar and advanced very high resolution radiometer imagery. *J. Geophys. Res.*, **101** (C7), 16 391–16 400.

Nicholls, S., 1978: Measurements of turbulence by an instrumented aircraft in a convective atmospheric boundary layer over the sea. *Quart. J. Roy. Meteor. Soc.*, **104,** 653–676.

——, and C. J. Reading, 1979: Measurements of turbulence by an instrumented aircraft in a convective atmospheric boundary layer over the sea. *Quart. J. Roy. Meteor. Soc.*, **105,** 785–802.

——, and ——, 1981: Measurements of turbulence by an instrumented aircraft in a convective atmospheric boundary layer over the sea. *Quart. J. Roy. Meteor. Soc.*, **107,** 591–614.

Plant, W. J., 1982: A relationship between wind stress and wave slope. *J. Geophys. Res.*, **87C,** 1961–1967.

Rieder, K. F., 1997: Analysis of sea-surface drag parameterization in open ocean conditions. *Bound.-Layer Meteor.*, **82,** 355–377.

——, and J. A. Smith, 1998: Removing wave effects from the wind stress vector. *J. Geophys. Res.*, **103,** 1363–1374.

Robinson, I. S., 1985: *Satellite Oceanography*, Chap. 10–13, Ellis Horwood, 455 pp.

Robinson, S. K., 1991: Coherent motions in the turbulent boundary layer. *Annu. Rev. Fluid Mech.*, **23,** 601–639.

Smith, S. D., and Coauthors, 1992: Sea-surface wind stress and drag coefficients: The HEXOS results. *Bound.-Layer Meteor.*, **60,** 109–142.

Weissman, D. E., W. J. Plant, and S. Stolte, 1994: The modulation and coherence functions between atmospheric turbulence at the sea surface and the microwave radar cross section. *IGARSS 94*, Vol. 2, ESA Scientific & Technical Publications Branch, 791–794.